POLITECNICO DI TORINO

Master's Degree in Energy and Nuclear Engineering

Politecnico
di Torino

Master's Degree Thesis

Computational Modelling of Laser-Matter Interaction through EPOCH PIC Code in the Context of Inertial Confinement Nuclear Fusion

Supervisors

Prof. Roberto BONIFETTO

Prof. Antonio FROIO

Prof. Raffaella TESTONI

Candidate

Antonio ZURZOLO

October 2023

Contents

Abstract

The interaction between laser and matter is gaining increasing attention due to its diverse applications. These encompass a wide range of areas, including inertial confinement fusion for energy production, particles acceleration, medical diagnostics, and cancer treatment. Of particular significance is the proton-boron fusion, which offers the advantage of minimal high-energy neutron production, thereby reducing the potential hazard caused by neutron activation of surrounding materials.

Understanding the laser-matter interaction and having a comprehensive overview of the generated plasma's characteristics is fundamental. This thesis aims to simulate the interaction between lasers and matter using a particle-in-cell model. The ultimate goal is to simulate a target, specifically in the context of proton-boron fusion. The focus lies on the interaction between the laser and the primary target (pitcher) in a pitcher-catcher configuration for plasma fusion.

Before delving into simulations, a theoretical overview of plasma is provided, with particular emphasis on plasmas generated through lasers and their unique characteristics. Following the theoretical analysis, simulations are conducted, beginning with a comparison of results obtained with a scientific paper to validate the outcomes. Subsequently, simulations of the pitcher, composed of plastic and boron materials, are performed. The pitcher's objective is to generate a high-energy proton beam that will interact with the secondary target (catcher).

Several simulations are conducted, varying different parameters that affect the generated plasma, including laser intensity, angle, and pulse duration. These simulations reveal how changes in these parameters alter the plasma's characteristics. Notably, they highlight the importance of achieving the correct laser intensity and pulse duration to generate a fully ionized plasma. Furthermore, an increase in the laser's polarization angle is shown to increase the energy absorbed by the target, resulting in higher-energy particles exiting the system.

"In the middle of every difficulty lies opportunity".
Albert Einstein

Introduction and Goals

In the current scientific context, interactions between lasers and matter have assumed an increasingly prominent role, permeating various disciplines and opening new perspectives in technological and scientific applications. Over the past few decades, laser intensity has significantly increased, enabling the generation of laser pulses on the order of attoseconds. This has created opportunities for various laser applications, particularly in the field of energy production, specifically in the context of inertial confinement fusion. When a high-intensity laser interacts with a target, rapid matter ionization occurs, leading to the creation of a high-energy plasma where particle temperatures reach the order of MeV. This has made laser-based proton-boron fusion an intriguing prospect. Unlike traditional deuterium-tritium fusion, proton-boron fusion has a lower interaction cross-section and releases less energy. However, it avoids the production of high-energy neutrons, which can activate materials and render them radioactive. Furthermore, hydrogen and boron, the reactants in this fusion process, are stable elements readily available without the need for in-situ production, unlike radioactive tritium. Another intriguing aspect is that proton-boron fusion releases only charged particles, which could be exploited for direct energy production, potentially increasing energy production efficiency. To achieve these objectives, it is crucial to understand the interaction between lasers and matter and simultaneously characterize the generated plasma. Computational simulations through computer models, in addition to laboratory experiments, are essential tools for gaining a quantitative understanding of the physical processes governing laser-matter interactions. These processes include laser beam absorption, energy exchange with the target material, especially between electrons and ions, fusion reactions, and ionization of target atoms. The primary goal of this thesis is to simulate the interaction between a laser beam and matter, with the aim of analyzing the characteristics of the confined plasma and determining the optimal target configuration to maximize energy absorption. The research explores the effects of target materials and size on plasma parameters and energy absorption. Additionally, given the fundamental role of ionization in plasma generation, the study evaluates how different ionization mechanisms influence the quantity of generated free electrons. The ultimate objective is to focus on proton-boron fusion,

particularly by analyzing a common target configuration known as the "pitcher-catcher." This configuration consists of two targets: a pitcher and a catcher. The pitcher, impacted by the laser beam, generates a high-energy proton beam that, upon interaction with the catcher composed of boron, initiates fusion reactions. To achieve these goals, a Particle-in-Cell (PIC) code has been employed as a computational tool capable of simulating extensive systems of interacting particles. The chosen software for this purpose is EPOCH, an open-source program. Before delving into computational analysis using the PIC model, **chapter 1** examines the characteristics of plasma generated by laser-matter interactions. It also provides an overview of lasers and laser-matter interactions, with a specific focus on laser-induced ionization processes and target energy absorption. In **chapter 2**, the thesis describes the PIC model, explaining its utility in simulating laser-matter interactions and its key features. **Chapter 3** presents an attempt to replicate previous research results to familiarize with the software and ensure the correctness of the methodology. Specifically, the simulations involve the self-heating process that characterizes PIC models, resulting in a non-physical linear temperature increase. It has been demonstrated that this effect can be mitigated by using current smoothing and increasing the number of particles per cell. Additionally, simulations were conducted to test the performance of the collision module in EPOCH. For instance, it has been observed that a non-equilibrium distribution can be thermalized through self-collisions; and an initially anisotropic thermal distribution can be rendered isotropic as a result of collisions. In **chapter 4**, the research applies the PIC tool to simulate various new target configurations composed of various materials. Particular emphasis has been placed on a boron-based pitcher target with a polystyrene substrate. In fact, the last target under analysis is related to inertial confinement fusion, specifically the Proton-Boron fusion, which occurs through the following reaction:

$$p + {}^{11}B \longrightarrow 3\alpha + 8.7\text{MeV} \tag{1}$$

This is classified as an aneutronic fusion process, meaning it does not produce highly energetic neutrons, which are considered undesirable byproducts in classical D-T (Deuterium-Tritium) fusion reactions. In D-T reactions, these energetic neutrons can activate surrounding materials, resulting in the production of radioactive waste. Proton-Boron fusion, on the other hand, involves stable and readily available elements like Hydrogen and Boron. In contrast, D-T fusion uses Tritium, a radioactive material with a half-life of approximately 12 years. This means that even if Tritium is produced in a breeder, after 12 years, only half of the produced amount remains. This radioactive nature of Tritium is a significant drawback of D-T fusion. Additionally, Proton-Boron fusion generates only charged particles, which can be

directly utilized to produce energy, enhancing the efficiency of the fusion process. Beyond its applications in the energy sector, Proton-Boron fusion holds promise for various other applications, such as producing medical radioisotopes and conducting particle physics experiments involving the acceleration of particles to relativistic speeds. [1]

The target was analyzed to understand how different laser parameters, such as intensity and polarization angle, modify the characteristics of the generated plasma and laser beam absorption by the target wall. Specifically, it has been shown that as the polarization angle increases, the energy absorbed by the wall increases as well. The temperatures reached by the electrons in the various simulations were evaluated, and the intensity and pulse duration required to fully ionize the target were verified.

Chapter 1

Laser generated plasma

Plasma is the most abundant state of matter in the universe, but it is limited on Earth. It is the energy source of stars, and on Earth, it can be formed by the interaction between the solar wind and the Earth's magnetic field, which is known as the aurora borealis, or more commonly, in lightning (**figure 1.1**). It is often referred to as the fourth state of matter, although it can exist in gaseous, liquid, and even solid phases. Its unique properties justify its identification as a distinct state of matter. This chapter provides a brief overview of plasma, highlighting its main properties. However, the primary focus will be on plasmas generated through the interaction between high-power lasers and matter.

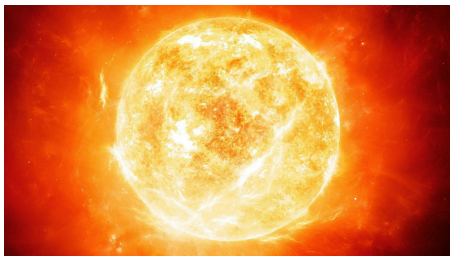

(a) sun

(b) lightning

(c) aurora borealis

(d) plasma lights

Figure 1.1: Examples of plasma in space and on Earth [2, 3, 4].

1.1 Unravelling Plasma: Behaviors and Unique Features

In physics, plasma is a fully or partially ionized gas, meaning that it is composed of free electrons and ions. Any substance can become plasma by increasing its temperature because extracting an electron from an atom requires energy greater than the binding energy of the electron. Additionally, this energy must be sufficient to overcome recombination phenomena, which tend to rejoin electrons and ions. Focusing on a hydrogen atom, the energy required for its ionization is given by the Rydberg constant ($Ry = 13.6$ eV). However, due to the tail in the Maxwell distribution of velocities, this threshold energy can be reduced to about 1 eV. This is because the velocities of particles in a gas are different from each other and are described by the Maxwell distribution. Some particles in the gas may have enough kinetic energy to ionize the atoms even at low temperatures. [5, 6]

Referring to a gas in thermal equilibrium, the amount of ionisation is given by the Saha equation which defines the ratio between the density of ionised atoms (n_i) over the density of neutral atoms (n_n):

$$\frac{n_i}{n_n} \approx 2.4 \cdot 10^{21} \frac{T^{\frac{3}{2}}}{n_i} e^{-\frac{U_i}{K_B T}} \tag{1.1}$$

where T is the temperature in Kelvin, U_i is the ionization energy, which depends on the type of atom, and K_B is the Boltzmann constant. As can be seen from the equation, raising the temperature increases the ratio n_i/n_n leading to more ionized atoms compared to neutral ones. This results in a plasma state. Additionally, maintaining a plasma state requires low density and a vacuum environment. Otherwise, air cools down the plasma and ions and electrons recombine to form a normal gas. At room temperature, the ratio in the Saha equation is very low. Additionally, there is no vacuum on Earth, which explains why we can only experience plasmas in very few examples (**figure 1.1**). [7]

The previous definition of plasma as a fully or partially ionized gas is not entirely accurate, as not all ionized gases exhibit plasma behaviour. To qualify as plasma, an ionized gas must demonstrate collective behaviour.

Imagine a gas in a state of thermal equilibrium. If a disturbance is introduced into this system, it spreads through particle collisions. Consequently, any alterations in the system are tied to short-range forces, such as Van Der Waals forces (proportional to r^{-6}). However, in the case of a plasma, composed of charged particles, introducing a disturbance results in its propagation via Coulomb interactions between particles. These interactions are long-range forces (proportional to r^{-2}). In this scenario, charged particles can interact with multiple particles over significant distances, defining the collective behaviour of plasma. In conclusion, the definition of plasma

can be stated as: *"A plasma is a quasi-neutral gas of charged and neutral particles that exhibits collective behaviour"*[7].

One of the primary attributes associated with plasma, which arises from its collective behaviour, is its ability to shield an imposed potential. Imagine an infinite neutral plasma where the density of ions (n_i) equals the density of electrons (n_e). If a charge (Q) is introduced into this plasma, it will attract oppositely charged particles while repelling those of the same charge. Consequently, a concentration of particles will gather around the charge (Q), working to neutralize the electric field generated by the charge. The interaction between charged particles follows Coulomb scattering, which depends on particles' kinetic energy. Higher kinetic energy results in weaker interaction. This means that as the plasma's temperature increases, the shielding of the applied potential diminishes, and conversely. In a theoretical scenario of a cold plasma with particles devoid of thermal motion, the potential shielding would be perfect, and the charge's accumulation would impact an infinitesimal area. This phenomenon is termed Debye shielding, which maintains charge neutrality within the plasma bulk (where $n_e = n_i$). Despite an applied external potential, the electric field within the plasma remains negligible, except within a spatial region defined by the Debye length (λ_d). The Debye length can be defined as the distance across which the plasma can shield an applied potential. [8, 7] Mathematically, the Debye length (λ_d) is given by the equation:

$$\lambda_d^2 = \left(\frac{\epsilon_0 K_B T_e}{e^2 n_e}\right) \tag{1.2}$$

Here K_B is the Boltzmann constant, ϵ_0 the vacuum permittivity, e the electron charge, T_e and n_e the electron temperature and number density respectively. This formula pertains to the Debye length for electrons. In general, a plasma is not in thermal equilibrium; the electrons possess higher kinetic energy compared to the ions, leading to different temperatures between the two. Consequently, the Debye length will be different for the two particles. It's evident that as temperature increases, (λ_d) expands, affirming the prior explanation. Moreover, (λ_d) is inversely proportional to the electron density (n_e). Considering the parallel contribution of both electrons and ions the following expression can be written [8]:

$$\frac{1}{\lambda_d^2} = \frac{e^2 n_e}{\epsilon_0 k_b T_e} + \frac{e^2 n_i}{\epsilon_0 k_b T_i} \tag{1.3}$$

The response of a plasma system to an applied potential has previously been characterized in spatial terms, as indicated by the Debye length. Now, a similar analysis can be conducted in the temporal domain. When a plasma system is perturbed, it will tend to restore its original configuration after a short period of time. To define the system's time response, one can consider a minor perturbation where the condition $e\Phi \ll K_B T$ holds true. This means that the energy of electrons

is relatively close to the thermal energy. Consequently, the electron velocity aligns closely with the thermal velocity. By employing this perspective, the time necessary to shield an applied potential can be defined. Given that the shielding distance is denoted by λ_d and the velocity corresponds to the thermal velocity, the time required to restore equilibrium can be approximated as $\tau \approx \lambda_D / v_e$. The parameter τ represents the time needed for reestablishing equilibrium. The reciprocal of τ corresponds to the electron plasma frequency, often referred to as the plasma frequency ω_p.

$$\omega_p = \frac{v_e}{\lambda_D} = \sqrt{\frac{n_e e^2}{\epsilon_0 m_e}} \tag{1.4}$$

Concluding, the criteria necessary to have a plasma are:

- $L \gg \lambda_d$
- $N_D \gg 1$
- $\tau > \omega_p$

Considering L the dimension of the system, it must be much greater with respect to the Debye length to ensure charge neutrality. Moreover, the number of particles in a Debye sphere (N_D) [1] has to be adequate otherwise the description of Debye shielding we made above is not valid anymore. Moreover, since the time response of the system is given by the plasma frequency ω_p, the time response of the system to a perturbation is given by $\tau = 1/\omega_p$, this lead to the last statement since to have a plasma its lifetime has to be greater than the reciprocal of the plasma frequency. [8, 7]

1.2 Laser technology

The advent of lasers traces back to 1960, although the theoretical groundwork dates back to Einstein's work on stimulated emission of radiation in 1916. The term LASER stands for **L**ight **A**mplification by **S**timulated **E**mission of **R**adiation, underscoring the fundamental role of stimulated emission in laser technology. Stimulated emission involves a photon interacting with an atom in an excited state, causing it to transition to a lower energy state and emitting an additional photon with identical direction and frequency (**figure 1.2**). [9]

[1] N_D represents the number of particles in a Debye sphere. Referring to the electrons: $N_D = \frac{4}{3}\pi\lambda_{De}^3 n_e$

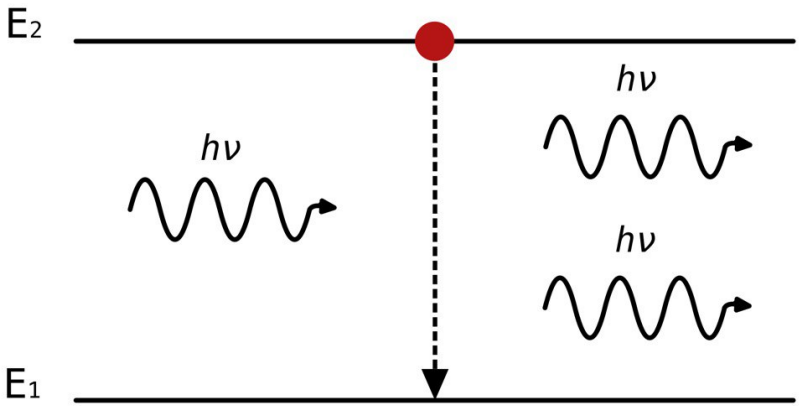

Figure 1.2: Illustration of stimulated emission: the picture shows two energy levels, E_2 and E_1, where $E_2 > E_1$. A photon having energy $h\nu$ interacts with an atom in state E_2, this interaction leads to the transition of the atom to the state E_1 with the emission of another photon along with the first one. Note that $E_2 - E_1 = h\nu$.

A laser system typically comprises an active material, pumping devices, and an optical cavity. The active material enhances photon population through stimulated emission, while pumping devices facilitate population inversion, where the higher energy level becomes more populated than the lower level. This inversion ensures a greater number of photons are emitted through stimulated emission. The optical cavity, consisting of mirrors, maximizes photon population by reflecting photons multiple times within the active material. This enhances laser emission efficiency. Since its inception in the 1960s, laser technology has steadily advanced (**figure 1.3**). A significant leap occurred in the 1990s with the development of Chirped Pulse Amplification (CPA) lasers, pioneered by Strickland and Mourou, who were honoured with the Nobel Prize in 2018 for their contributions [10]. CPA technology has enabled the attainment of intensities approaching 10^{22} W/cm^2. Through mode-locking techniques, peak power can be elevated to around 10^{24} W/cm^2 in femtoseconds pulse durations. This remarkable progress has substantially elevated the achievable maximum laser intensity. This breakthrough has wide-ranging implications for laser-plasma interaction applications.

One application that has benefited from the increased peak power of a laser is inertial confinement fusion. High-energy laser beams, when interacting with solid or gaseous matter, immediately ionize the matter constituents. This leads to the generation of a highly ionized gas consisting of electrons and ions that can move freely while maintaining overall neutrality. This system of particles is known as plasma. If the energy of the laser beam incident on the target is sufficiently high, the kinetic energy of the particles increases to the point where it overcomes

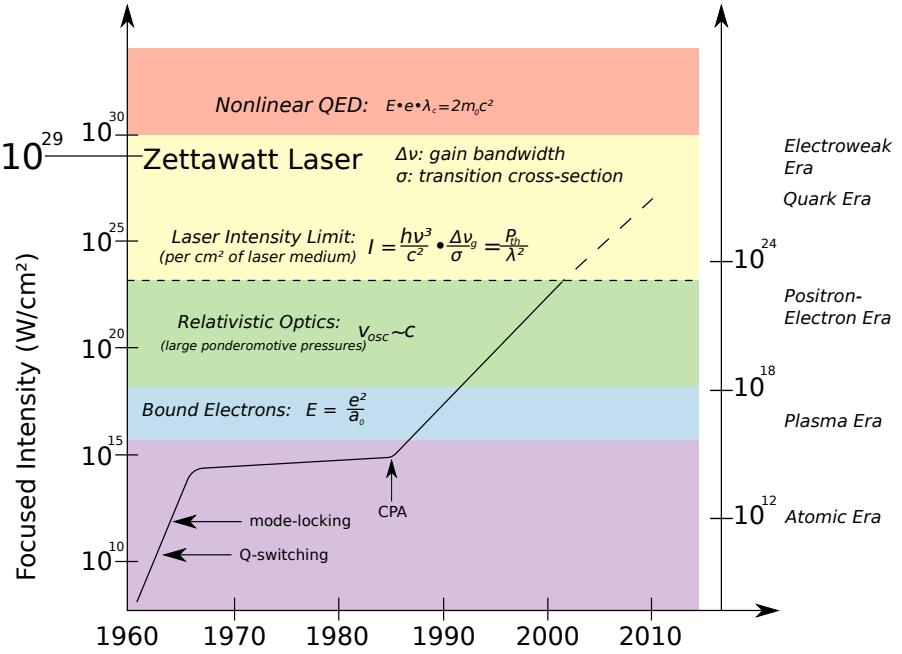

Figure 1.3: The picture shows the progression of laser technology, with a notable surge around 1990 attributed to the innovation of the CPA technology [11].

the Coulomb repulsion between particles of the same charge. This makes the dominant force the strong nuclear interaction, allowing the fusion of light nuclei such as deuterium and tritium. Moreover, when laser power densities exceeds 10^{18} W/cm^2, plasma particles can be accelerated to relativistic velocities. This innovation opens avenues for using lasers as more compact particle accelerators, expanding the potential applications of laser-plasma interaction.

A high-intensity laser can be generated by concentrating a significant amount of energy within a brief time span and directing the light onto a confined area. The primary challenge encountered with lasers before 1990 was the degradation of the active material at high intensities. This problem was resolved with the development of the Chirped Pulse Amplification (CPA) technique, comprising three phases: stretching, amplification, and compression. Initially, the laser pulse is extended in time (chirped pulse), thereby lowering the peak intensity avoiding the degradation of the active material. In the subsequent phase, the chirped pulse passes through the active material to amplify the laser emission. In the final stage, the amplified chirped pulse is compressed temporally, resulting in a short pulse with an exceptionally high peak intensity. Subsequently, the laser beam is focused onto a confined spatial area (**figure 1.4**). [9]

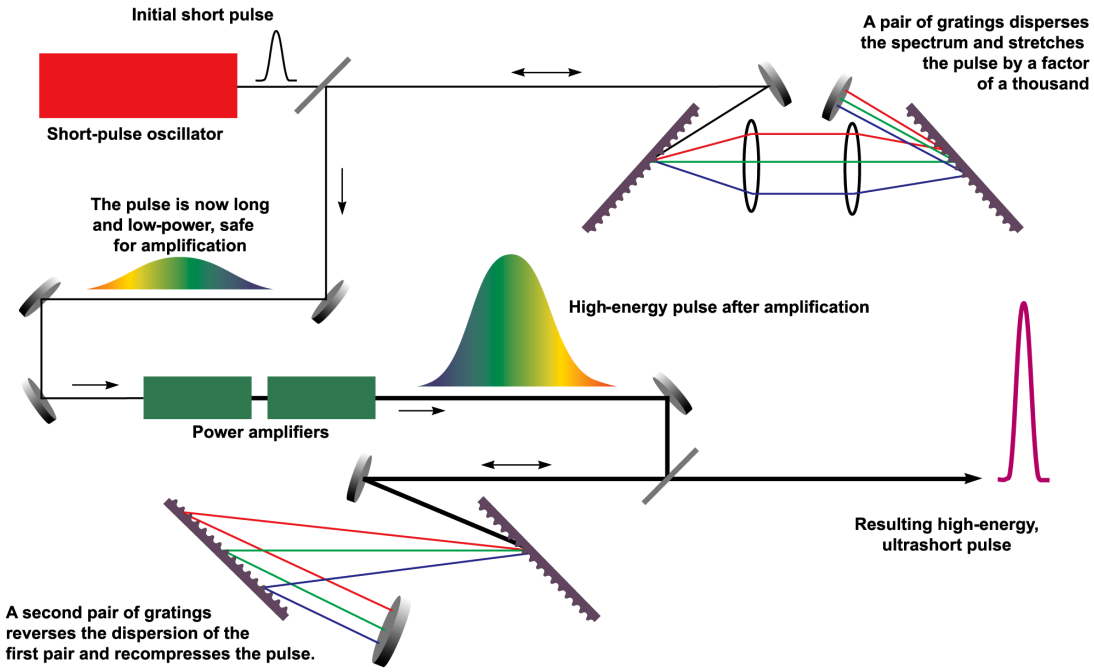

Figure 1.4: Scheme of Chirped Pulse Amplification (CPA) technique [12].

1.3 Laser propagation

From a quantum perspective, a laser beam can be regarded as a collection of photons, each possessing energy proportional to their frequencies according to the equation $E = h\nu$. Therefore, the energy of the laser beam can be expressed as $I = n_{photon}\ h\nu\ c$ where $n_{photons}$ represents the number density of photons, h is the Plank constant and c the speed of light. In the framework of wave-particle duality proposed by De Broglie, a photon can also be viewed as a wave characterized by frequency ν, wavelength λ, and velocity c. In the context of laser-plasma interaction, when the photon number density is substantial (approximately 10^{12} photons/cm^3 for $\lambda = 1$ µm), the behaviour of photon flow can be effectively described using classical electrodynamics. Generally, this condition is applicable in laser-plasma applications. [13]

The electric field of a linearly polarized laser beam propagating along the z-direction can be expressed in a general form as follows:

$$E(x, y, z, t) = A(x, y, z)e^{i(kz-\omega t)} \tag{1.5}$$

In the case of a laser, the spatial profile can be closely approximated using a Gaussian function. In **equation** (1.5), the function A defines the spatial profile of

the electric field. Specifically, for a Gaussian beam, this function can be expressed as:

$$A(x,y,z) = E_0 \frac{w_0}{w(z)}\ e^{\frac{-r^2}{w(z)^2}}\ e^{\left[i\frac{kr^2}{2R(z)}+i\phi(z)\right]} \tag{1.6}$$

The variable r signifies the radial distance from the central axis of the beam. The symbol i represents the imaginary unit. E_0 corresponds to the electric field at the origin of the beam, situated at coordinates $(r = 0, z = 0)$. The wave number k is defined as $k = \frac{2\pi}{\lambda}$, while $\phi(z)$ denotes the phase. The essential parameters for describing a laser beam are the beam waist, denoted as $w(z)$ and the curvature radius of the beam's wavefront, labelled as $R(z)$ (**figure 1.5**). These last parameters are defined as:

$$R(z) = z\left[1 + \left(\frac{\pi w_0^2}{\lambda z}\right)^2\right] \tag{1.7}$$

$$w(z) = w_0\left[1 + \left(\frac{\lambda z}{\pi w_0^2}\right)^2\right]^{\frac{1}{2}} \tag{1.8}$$

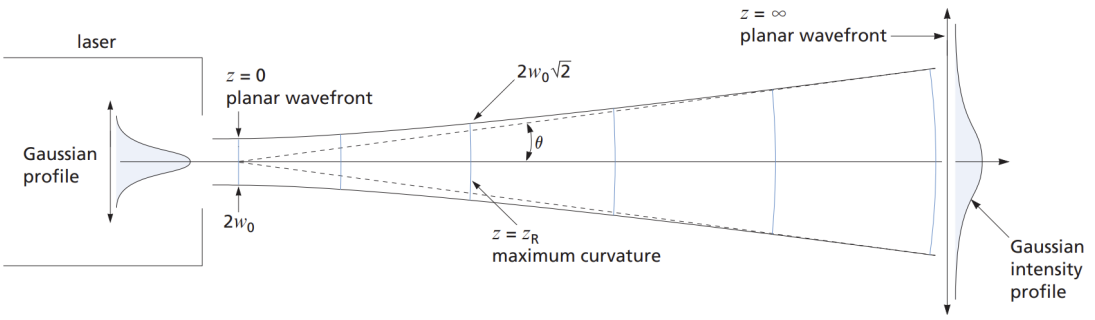

Figure 1.5: The illustration depicts the laser's propagation originating from the emission point. It is observable how the beam's radius enlarges along the direction of propagation, which is described by the beam waist denoted as w(z) [14].

Despite the laser being collimated, diffraction induces the spreading of waves in a direction transverse to the propagation direction. The extent of diffraction curvature is determined by the curvature radius $R(z)$. Meanwhile, the beam waist $w(z)$ signifies the radius of the beam at a specific distance z in the propagation direction. Due to the presence of diffraction, the beam waist changes and gradually increases along z. Its smallest value occurs at z=0, which designates the focal point of the laser beam. Another significant factor in describing a laser beam is

its intensity, denoting the energy released per unit area. The intensity is directly proportional to the square modulus of the energy, and it can be reformulated as follows:

$$I(r,z) = I_0 \left(\frac{w_0}{w(z)} \right)^2 e^{\left(\frac{w_0}{w(z)^2} \right)} \tag{1.9}$$

[13, 14, 15]

The parameters discussed earlier play a fundamental role in laser beam characterization and exert a substantial influence on the interaction between lasers and matter. A comprehensive description of a Gaussian laser beam can be found in references [16]. A detailed explanation of the beam quality factor M^2, which is a parameter to quantify deviations from an ideal Gaussian beam, is available in references [14, 17]. Various spatial and temporal profiles can characterise a laser beam. For a deeper understanding of the prevalent shape functions concerning laser spatial/temporal profiles, such as the top hat function and Bessel function, one can refer to references [16] and [13].

1.4 Laser-Matter interaction

In the previous section, it has been discussed that when a laser beam comes into contact with matter, it swiftly causes the atoms within the matter to become ionized. This ionization occurs because the laser beam releases energy to matter, and the extent of this energy transfer depends on the intensity of the laser. This interaction involves numerous physical phenomena. The forthcoming section, will concern on the description of the most significant phenomena which characterize the interaction between high-intensity, short-pulse lasers and solid materials. One of the key factors influencing this interaction is the density. As a result, the nature of the interaction varies depending on whether the matter is solid or gaseous. Notably, when dealing with a solid target, an overdense plasma comes into play. An overdense plasma is characterized by a high number of particles per volume [18].

When a high-power laser interacts with a solid target, it triggers swift atom ionization through either direct photo-effect or multiphoton processes. For an atom to be ionized through direct photon-electron interaction (photo-effect), a substantial amount of energy is required, as the energy carried by the incoming photon must exceed the electron's binding energy. Hence, ionization by multiphoton processes is more commonplace. The resulting electrons are subsequently heated either by localized absorption or inverse Bremsstrahlung. These electrons then expand into the vacuum, confined by the potential created by the laser beam. This expansion takes place over a distance defined by the Debye length, where charge separation

occurs. Consequently, during the duration of the laser pulse, only electrons undergo heating, while ions remain largely stationary, leading to minimal impact on ion density. Following the generation of a certain quantity of electrons via photon processes, a chain reaction of ionization unfolds, with highly energetic electrons ionizing atoms through collisional interactions. For direct interaction between the laser and matter, a density lower than the critical density is requisite. This critical density is significantly below solid density (approximately 100 times lower). Upon reaching the critical density, the propagation of the laser becomes untenable, marking the onset of a complex interplay of diverse phenomena in the interaction between the laser and matter.

In the initial stages, the plasma is dominated by collisional behavior, characterized by processes such as collisional absorption or inverse Bremsstrahlung. As the plasma's temperature rises, it transitions into a predominantly collisionless state. The parameter that serves to gauge whether the plasma behaves collisionlessly is the mean free path, which can be expressed as follows:

$$l_{ei} \approx 3 \times 10^{13} \frac{\epsilon^2}{Z n_e} \text{ cm} \tag{1.10}$$

Where ϵ is the energy in eV, Z the atomic number and n_e the electron density. When dealing with ultrashort laser pulses, the mean free path is shorter than the laser penetration length. As a result, absorption will be collisionless. As the temperature rises, the mean free path extends, causing the plasma to shift into a collisionless behavior. [18, 5, 19]

1.4.1 Critical density

When electromagnetic radiation traverses through a medium, its characteristics undergo alteration compared to when it travels through free space. This modification in properties within the medium is elucidated by the dispersion relation. For electromagnetic waves within a plasma, the dispersion relation is expressed as follows:

$$\omega^2 = c^2 k^2 + \omega_p^2 \tag{1.11}$$

In this equation, given a value for either k or ω, the other is not independent but must satisfy the above relation for wave propagation to occur. As illustrated in **equation** (1.4), ω_p's value is reliant on density. Consequently, when plasma density increases, so does the plasma frequency. However, this elevation must comply with **equation** (1.11), thereby requiring k to diminish until it reaches zero. At this point, the incoming radiation's frequency equals the plasma frequency ($\omega = \omega_p$), leading to reflection of the laser beam. The state $\omega = \omega_p$ is referred to as the cut-off frequency, with the corresponding density termed critical density n_c.

Whenever the laser frequency is subordinated to the plasma frequency, the laser beam cannot effectively traverse the medium and is consequently reflected. To increase the laser's path within the medium and thereby expand the interaction area, the angle of incidence for the laser beam can be augmented. This outcome results from the existence of a density gradient. When an electromagnetic radiation impinges obliquely upon this gradient, it encounters lower density at the point of reflection. This in turn elongates the path that the radiation takes through the medium. However, it's important to remark that these reflections occur at a density level below the critical density. [5, 18]

1.4.2 Ionization phenomena

As previously indicated, the initial interaction results in the ionization of atoms, giving rise to the emission of electrons. In the first femtoseconds, the principal mechanism driving ionization is the interaction with the laser's electric field, leading to what is known as field ionization. Subsequently, as time progresses, collisional ionization becomes predominant, occurring when electrons collide with ions or atoms. [20]

When considering a laser beam exhibiting intensities on the order of petawatts, the electric field generated in the laser's focal point surpasses the inherent atom field strength. This atom field strength can be computed as follows:

$$E_a = m_e^2 e^5 \hbar^{-4} \approx 5.1 \times 10^9 \mathrm{V/cm} \tag{1.12}$$

Here, e and m_e denote the electron's charge and mass, respectively, and $\hbar$ signifies the reduced Planck constant. In this scenario, atoms experience the influence of the laser field, which triumphs over the atom's internal field, thereby enabling the extraction of electrons from the atom, leading to ionization. The process of field ionization encompasses several distinct phenomena contingent upon the magnitude of the applied electric field:

- **Multiphoton ionization** occurs when E is significantly less than E_k
- **Tunnel ionization** takes place when E_k is considerably smaller than E, but still less than E_{cr}
- **Barrier suppression ionization** manifests when E surpasses E_{cr}

Here, $E_k = \omega_L (2 m_e I_i)^{1/2} / e$ denotes the field associated with the Keldysh parameter γ, as defined below (**equation** (1.14)). In this equation, I_i represents the ionization potential of the atom, ω_L signifies the laser frequency, and E_{cr} indicates the threshold electric field magnitude at which barrier suppression ionization takes effect. [21]

$$\gamma = \frac{\omega\sqrt{2m_e\epsilon}}{eE} \tag{1.13}$$

Multiphoton ionization is as a nonlinear mechanism of photon absorption, involving the excitation of electrons from their ground state into a virtual quantum state multiple times. As these electrons accumulate sufficient energy, they are liberated from the atom, thereby inducing ionization. Essentially, an electron interacts with multiple photons, each possessing energy lower than the electron's ionization energy (ϵ_{ry}). Consequently, if through the process of multiphoton interaction an electron absorbs a total energy equal to or greater than its ionization energy, it is then emitted from the atom. This phenomenon exhibits nonlinear behavior and presents challenges in prediction. To address this, the time-dependent Schrödinger equation must be solved. Its numerical solution leads to the formulation of the uncertainty principle, as depicted below:

$$\Delta\epsilon \cdot \Delta t = \frac{\hbar}{2} \tag{1.14}$$

The equation provided above is useful to evaluate the condition under which an electron is emitted by multiphoton ionization. In reference [5], it has been demonstrated that under a laser intensity of $1 \times 10^{15}\,\mathrm{W/cm^2}$, 14 photons with an energy of 1 eV can extract an electron within a time span of 5 fs. Consequently, interaction with photons must occur within this timeframe to ensure successful emission. Otherwise, the electron might relax by emitting additional photons, thereby impeding the attainment of ionization energy. [5] Furthermore, as previously noted, the prevalence of multiphoton ionization becomes pronounced when $\gamma >> 1$. Examining the definition of γ, it becomes clear that this condition holds true at high frequencies and low field strengths of laser radiation. Under these circumstances, multiphoton ionization prevails over tunneling ionization. [22]

In contrast, **tunneling ionization** emerges as the predominant phenomenon when confronted with low frequency and high field strength scenarios. As a result, it is anticipated that the initial phase is primarily governed by multiphoton ionization, with tunneling ionization expected to occur subsequently. With laser intensities surpassing the petawatt per square centimeter range, tunneling ionization takes center stage. Tunneling ionization involves a quantum mechanical occurrence wherein an electron possesses a nonzero probability to tunnel through the atom's Coulomb barrier under the influence of a strong electric field. This phenomenon occurs under the same conditions as multiphoton processes but within a different energy range. For a more comprehensive understanding, including the rate of ionization through tunneling effects, one can refer to reference [22].

As the magnitude of the electric field (representing the laser intensity) further escalates, the Coulomb barrier can be surmounted. In such cases, the phenomenon

is termed **over-the-barrier** ionization or **barrier-suppression ionization**. **Figure 1.6** illustrates a comparison among the three ionization regimes.

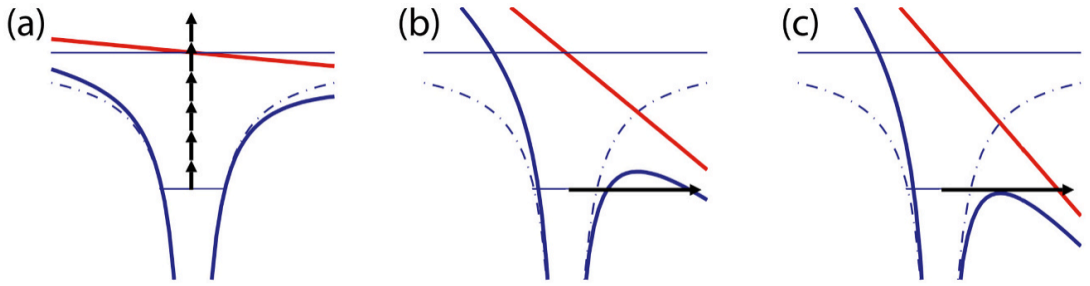

Figure 1.6: The illustration depicts a schematic overview of the three ionization mechanisms. The vertical axis denotes energy levels, while the horizontal axis signifies position. The dashed-dotted line portrays the Coulomb potential in the absence of an external field, the blue line is the Coulomb potential under the influence of the external field, and the red line represents the electric field of the laser beam. In panel (a), the depiction stands for multiphoton absorption, wherein an atom absorbs multiple photons leading to the expulsion of an electron. Panel (b) illustrates tunneling ionization, involving the electron's passage through the Coulomb potential subsequent to photon absorption. Panel (c) outlines barrier-suppression ionization, where the Coulomb barrier's suppression enables the electron to break free from the atom.[23]

As time advances, **collisional ionization** becomes more pronounced. In this process, electrons absorb energy from the laser beam and trigger atom ionization through collisions. This mechanism is relatively straightforward: when a high-energy electron collides with an atom or ion, and the exchanged energy exceeds the atom's binding energy, the atom or ion releases an electron, resulting in ionization.

1.4.3 Plasma absorption mechanisms

The mechanisms of plasma-laser absorption can be categorized into two types: collisional and collisionless (or collective). In collisional mechanisms, the Coulomb interaction governs the process, wherein the energy of the photons transforms into energy of the particles comprising the matter, due to the Coulomb field of individual particles. Conversely, collisionless behavior hinges on resonant interaction with collective fields.
For *long-pulse lasers*, the energy from the laser pulse is transferred to the plasma through *collisional processes*, such as inverse Bremsstrahlung. On the contrary, *short-pulse lasers* predominantly heat the plasma via *collisionless phenomena*. In the contest of inertial confinement fusion short pulse lasers are the most promising

to trigger on the fusion reaction since they could reach very high intensities. As a result, this section will exclusively describe collisionless phenomena.

Among the various phenomena, the following hold particular relevance:

Resonance Absorption: This is an important heating mechanism in short-pulse laser-matter interactions, especially for plasmas with solid densities, where electron density greatly exceeds the critical density. Such plasmas exhibit high reflectivity due to early critical density attainment, resulting in $\omega = \omega_p$. When considering a p-polarized electromagnetic wave with oblique incidence, resonance absorption becomes effective when the laser frequency aligns with the plasma frequency. Although oblique incidence leads to laser beam reflection at lower densities, critical density can still be reached via tunneling, where resonance absorption will be more effective with respect to a laser beam perpendicular to the target. Within the critical layer, a plasma wave (Langmuir wave) is excited, and resonance drives this wave to attain substantial amplitude until it can no longer be sustained and is abruptly damped (wave breaking occurs). The damping mechanism depends on the incident laser beam's intensity. At relatively low intensities ($< 10^{14}\,\mathrm{W/cm^2}$), collisional damping occurs. As energy increases, Landau damping mechanisms become dominant. With further intensity escalation, nonlinear Landau damping takes precedence.

Ponderomotive Acceleration: This phenomenon drives charged particles away from high-intensity zones. Consequently, electrons migrate from regions with peak electric field amplitudes, enabling energy transfer to regions distanced from peak intensity. The non-relativistic ponderomotive force acting on charged particles in an electric field can be expressed as:

$$F_p = -\frac{q^2}{4m\omega^2}\nabla E_0^2 \tag{1.15}$$

Importantly, it is independent of particle charge, also expelling ions from high laser intensity zones. Thus, ponderomotive forces can be seen as a radiation pressure, driving particles from high-intensity to low-intensity areas, akin to ordinary pressure.

$\mathbf{J} \times \mathbf{B}$ absorption becomes a significant heating mechanisms at high intensities ($> 10^{18}\,\mathrm{W/cm^2}$) when relativistic effects cannot be neglected. This force acts upon electrons due to the laser's magnetic field.
[18, 19, 24, 25]

Chapter 2

PIC code to simulate laser-plasma interaction

A plasma system can be modelled in various ways depending on the type of initialization condition. Two primary approaches are Magnetohydrodynamic (MHD) and Particle models. In the MHD approach, plasma is treated as a fluid subjected to electromagnetic fields with a Maxwellian distribution of the particles comprising the fluid. On the other hand, PIC codes utilize a statistical approach where plasma is treated as a sample of charged particles. PIC codes are mainly used to describe phenomena characterized by a non-Maxwellian distribution on a short timescale, ranging from picoseconds to femtoseconds. In this chapter the main reasons in the choice of using a PIC code for the simulation of the interaction between laser and matter will be described. Moreover, a detailed description of the code employed in the simulation will be provided.

2.1 Particle models to simulate plasma physics

Explaining why a numerical model is necessary to describe a physical phenomenon may not be necessary. However, it is important to justify the use of a Particle in Cell (PIC) code to accurately describe the interaction between laser and matter. The PIC code represents a form of particle model that serves as a computational tool to simulate large systems of interacting particles. Within the context of particle modelling, each individual particle is treated as a discrete entity, characterized by specific properties such as position, velocity, and mass. The behaviour of each particle is dictated by a set of physical laws or rules that govern the interactions between particles.

A suitable computational model must be chosen based on the specific physical

phenomenon being studied. In particular, it is necessary to consider the length scale and the nature of the phenomenon under investigation. For instance, in the case of studying the flow of water through a nozzle, it is unnecessary to consider the properties of each fluid particle. Instead, focusing on a fluid element would provide a reasonable evaluation of the collective behaviour of the fluid, while minimizing computational time. Furthermore, it is important to note that selecting the appropriate model is not solely a matter of computational cost. In the previously mentioned example, a detailed evaluation of the behaviour of individual particles could result in misleading outcomes. In fact, studying the behaviour of each particle individually would only reveal molecular vibrations and rotations in microscopic elements of the water, which are not representative of the collective behaviour of the fluid.

The choice of the most suitable computational model relies on the relevant physical length and timescales of the phenomena under investigation. The following table, sourced from reference [26], illustrates the characteristic timescales for various phenomena that can be studied with particle models.

As depicted in **table 2.1**, there are different types of particle models based on the number of particles considered in the simulation. However, it should be highlighted the fact that a simulation particle does not necessarily equate to a physical particle, as it can represent more than one physical particle. A group of physical particles characterized by certain common parameters are grouped in a computational particles, this lead to a reduction in the number of particles since a simulation with a number of particles equal to the number of real particles will be unfeasible. In molecular dynamic experiments, a one-to-one correspondence between physical and computer model particles is required since the short length and timescales of molecular motions are significant. However, to simulate a plasma generated by the interaction between laser and matter, one simulation particle can represent a group of physical particles. These may be sufficient for simulating a laboratory plasma system, such as plasma generated through the interaction between laser and matter. Such a plasma is mainly collisionless, and its length and timescales, as shown in **table 2.1**, are determined by the frequencies and wavelengths of natural plasma oscillations, namely the plasma frequency and the Debye length, respectively.

Referring to **table 2.1**, in the context of plasma simulations, L becomes the Debye length previously mentioned ad λ_d, while N_p the number of particles within a Debye cube. It is important to note that these are estimates for a generic collisionless plasma system.

$$N_d = n\lambda_d^3 \tag{2.1}$$

A plasma is composed of a huge number of particles, a direct simulation of the plasma behaviour is not feasible. However, to study the collective behaviour

of a plasma it is not necessary to consider the same number of particles of the physical plasma, since only what happens at lengths greater than the Debye length is of interest. Additionally, it is sometimes possible to significantly reduce the simulation domain, resulting in a smaller number of particles and still obtaining reliable results.

To accurately represent the collective behaviour of a collisionless plasma, three conditions must be satisfied: (I) the kinetic energy must be sufficiently greater than the macroscopic potential energy; (II) the collision frequency must be much lower than the plasma frequency; (III) the domain length must be much greater than the Debye length. A collisionless plasma is characterized by electrons and ions moving in their Coulomb fields with sufficient kinetic energy to prevent recombination. This means that the thermal kinetic energy KE is significantly greater than the microscopic potential energy PE.

$$\frac{Thermal\,kinetic\,energy\ \ (KE)}{Macroscopic\,potential\,energy\ \ (PE)} >> 1 \tag{2.2}$$

This ratio for laboratory plasmas is indeed Nd; to satisfy this condition, it may seem that a large number of particles is necessary, but the fundamental physics only requires KE >> PE, which can be achieved with $N_d \cong 10$. The same applies to the collisionless condition, which requires that the collision frequency (ν) is much lower than the plasma frequency (ω_p), also achievable with $N_d \cong 10$.

$$\frac{\nu}{\omega_p} \approx \frac{1}{N_d} \log N_d << 1 \tag{2.3}$$

The third condition required for correctly representing the collective behaviour of a collisionless plasma is having a domain length much greater than the Debye length. This condition can be fulfilled in many problems by using periodic models with $L = 50\lambda_d$. This explains why collisionless plasmas can be simulated using small values of N_d or small L/λ_d ratios. To ensure the validity of the above statements, it should be noted that the interaction down to infinitesimal charge separation is not of interest. Moreover, when using a spatial grid to simplify the calculation of fields, fields and forces at a length lower than a grid cell are not observable and are smoothed away. This reduces the collisional effects between particles without changing the long-wavelength behaviour. Another issue to consider when dealing with point particles is the well-known Coulomb singularity resulting from the $1/r^n$ dependence of the Coulomb collision law, where $n = 0, 1, 2$ in $1D, 2D$, and $3D$, respectively. This issue is resolved by using the Vlasov approximation, which leads to the definition of superparticles, which are finite-sized particles. According to

Vlasov, superparticles can be seen as a finite-sized cloud of electrons or ions, where the position of the superparticles is the centre of mass of the clouds and their velocity is the mean velocity of the clouds. Since the size of the particles is finite, the distance between particles is always nonzero, avoiding the Coulomb singularity. As the radius of the finite-sized particles becomes comparable to the Debye length, the collision cross-section and collision frequency diminish rapidly compared to those of point particles, thus enforcing the uncollisional behaviour of the plasma system. [26, 27, 28]

Table 2.1: Example of physical systems represented by particle models [26].

Example	Computer particles	Particle attributes	Physical			Computer model		
			N_p	L	T	N_p	L	T
1. *Correlated systems*								
Covalent liquids	Atoms or molecules	Strength constants related to quantum-mechanical dipole and quadruple interactions, mass, force, position, velocity	10^5	$10^5 - 8$	10^{-12}	10^3 - 10^4	10^{-8} - 10^{-9}	10^{-12}
Ionic liquids	Poaitive ions, Negative ions	Charge, mass, force, position, velocity, radius	10^5	10^{-8}	10^{-12}	10^3 - 10^4	10^{-8} - 10^{-9}	10^{-12}
Stellar cluster	Stars	Mass, position velocity, force, radius	10^2 -10^3	10^{17}	10^{15}	10^2 -10^3	10^{17}	10^{15}
Galaxy clusters	Galaxies	Mass, position, velocity, force, radius	10^4 -10^5	10^{23}	10^{17}	10^4 -10^5	10^{23}	10^{17}
2. *Collisionless systems*								
Collisionless plasma	"Superparticle" $\simeq 10^8$ electrons or 10^8 ions	Charge, mass, position, velocity, radius	10^9 -10^{12}	10^{-5} -10^{-2}	10^{-9} -10^{-12}	$< 10^5$	10^{-5} - 10^{-2}	10^{-9} - 10^{-12}
Galaxies - spiral structures	"Superparticle" $\simeq 10^6$ stars	Mass, position, velocity, radius	10^{10} - 10^{11}	10^{21}	10^{13}	$< 10^5$	10^{21}	10^{13}
3. *Collisional systems*								
Submicron Semiconductor devices (microscopic Monte-Carlo model)	"Superparticle" $= 10^4$ electron wavepackets	Charge, mass, position, wavenumber, radius	10^8	10^{-7}	10^{-10}	$< 10^5$	10^{-7}	10^{-10}
4. *Collision-dominated systems*								
Semiconductor devices (diffusion model)	"Superparticle" $= 10^4$ electrons or holes	Charge, position	10^9	10^{-6}	10^{-9}	$< 10^5$	10^{-6}	10^{-9}
Inviscid, incompressible fluids (vortex)	Vortex element	Vorticity, position	continuum	10^{-3} - 10^6	10^{-3} - 10^5	$< 10^5$	10^{-3} - 10^6	10^{-3} - 10^5

The previous text describe how it is possible to simulate a system made by a huge number of particles, potentially reaching 10^{20} in number, through computer simulations reducing particle numbers without compromising the system's underlying physics. Specifically, when dealing with interactions between lasers and plasmas - which feature charged particles moving in electric and magnetic fields - a PIC code is utilized, which will be described in detail in the following section (**section 2.2**). In particular, in the current work EPOCH PIC has been employed. It was developed collaboratively between the University of Warwick, Queen's University Belfast, and the University of Strathclyde in the United Kingdom. The initial focus of EPOCH was to study the interaction between ultra-intense laser pulses and plasma, but it has since expanded to include a wide range of plasma physics simulations. In fact, despite remains a suitable code to simulate collisionless plasmas generated by the interaction of short-pulse lasers with matter, it includes collisional algorithm to take in account collisions between particles, which become relevant in the case of lasers with a greater pulse duration. [29, 30]

In the following sections, a comprehensive description of a PIC code will be provided, focusing particularly on the EPOCH PIC code and its various features.

2.2 PIC core algorithm

2.2.1 Mathematical description

In this section, will be described the core of the PIC algorithm, starting from the fundamental equations.

As previously mentioned, plasma is composed of a vast number of particles, which makes it possible to describe their evolution using statistical laws. This description is called the kinetic description and is based on the Boltzmann equation (**equation** (2.4)). However, three assumptions must be satisfied to use this method:

- The system is considered a continuous medium
- Quantum effects are negligible, and classical statistical laws can be used
- Particle interactions can be described as binary collisions

The first condition is easily achieved in the current case due to the vast number of particles involved. In standard plasma systems, the second hypothesis can be considered valid. However, in laser-generated plasma, quantum effects may arise, and they are considered in modern PIC codes like EPOCH. Nevertheless, for the purpose of this discussion, we can assume the second hypothesis to be true. The third hypothesis, on the other hand, is valid as long as the interaction distance is much smaller than the mean free path.

Under these assumptions, the Boltzmann equation can be used to describe the evolution of the N particles in space and time.

$$\frac{\partial f_s(\vec{r},\vec{v},E,t)}{\partial t} + \left[\vec{v}\cdot\overrightarrow{\nabla}_r + \vec{a}(\vec{r})\cdot\overrightarrow{\nabla}_v\right]\ f_s(\vec{r},\vec{v},E,t) = \left(\frac{\delta f_s}{\delta t}\right)_{coll} \tag{2.4}$$

where f_s represents the number of particles per unit hypervolume (phase space volume) while s denotes the particle type. In other words, it represents the number of particles having a velocity around $v = (v_x, v_y, v_z)$, a position around $r = (x, y, z)$ at time t with energy E. $\vec{a}$ represent the acceleration, $\overrightarrow{\nabla}_r$ and $\overrightarrow{\nabla}_v$ the space and velocity gradient respectively. The collision operator represents binary collisions between particles within the system. The full description of the Boltzmann equation and the development of the collision operator can be found in reference [31]. A comprehensive explanation of the Boltzmann equation and the derivation of the collision operator is provided in reference [31].

However, for highly ionized gases such as plasmas, binary collisions can be disregarded since charge-charge interactions cannot be treated as collisions. Instead, the dominant contribution is given by Coulomb forces, which cannot be neglected. Hence, a collisionless kinetic equation, known as the Vlasov equation, is employed

in PIC codes. A comprehensive description of this system of equations can account for special relativistic effects. While these effects may be negligible in a generic plasma simulation, they become increasingly significant as the energy of the laser driving the plasma increases. The relativistic form of the Maxwell-Vlasov equations is reported below. [32]

$$\frac{\partial f_s}{\partial t} + \left[\vec{v} \cdot \overrightarrow{\nabla}_r + \frac{q_s}{m_s}\left(\vec{E} + \frac{\vec{v}}{c} \times \vec{B}\right) \cdot \overrightarrow{\nabla}_v\right] f_s = 0 \tag{2.5}$$

Here, the acceleration is expressed using the definition of Lorentz force. In **equation** (2.5) q_s represents the charge of the particle, m_s the particle mass, $\vec{E}$ is the electric field, $\vec{B}$ the magnetic field and c the speed of light. The Vlasov equation is subsequently coupled with Maxwell's equations (**equation** (2.6)), allowing for the evaluation of electric and magnetic fields. [33]

$$\begin{aligned} \nabla \times \overrightarrow{E} &= -\frac{\partial \overrightarrow{B}}{\partial t} \\ \nabla \times \overrightarrow{B} &= \frac{1}{c^2}\frac{\partial \overrightarrow{E}}{\partial t} + \frac{\vec{j}}{\epsilon_0 c^2} \\ \nabla \cdot \overrightarrow{E} &= \frac{\rho}{\epsilon_0} \\ \nabla \cdot \overrightarrow{B} &= 0 \end{aligned} \tag{2.6}$$

The parameters necessary to solve this set of equations are determined by the charge and current density ($\vec{\rho}$ and $\vec{j}$ respectively), which are computed from the distribution function f_s [33].

$$\rho(\vec{x}, t) = \sum_s q_s \int_{\mathbb{V}} f_s(\vec{x}, \vec{v}, t) d\vec{v} \tag{2.7}$$

$$\vec{j}(\vec{x}, t) = \sum_s q_s \int_{\mathbb{V}} \vec{v} f_s(\vec{x}, \vec{v}, t) d\vec{v} \tag{2.8}$$

In many situations, a simplification of the previous set of equations can be made under the assumption of a non-relativistic electrostatic model. This results in the Vlasov-Poisson system of equations. [26]

The Vlasov equation bacame:

$$\frac{\partial f_s}{\partial t} + \left[\vec{v} \cdot \overrightarrow{\nabla}_r + \frac{q_s}{m_s}\vec{E} \cdot \overrightarrow{\nabla}_v\right] f_s = 0 \tag{2.9}$$

The electric field is evaluated from Poisson's equation:

$$\nabla^2\Phi = -\frac{\rho}{\epsilon_0} \qquad \overrightarrow{E} = -\overrightarrow{\nabla}\Phi \tag{2.10}$$

The net charge density is determined from **equation** (2.7) as before.

2.2.2 Space-time discretization of Vlasov's equation

As previously mentioned in Section (**section 2.1**), the PIC code is based on the discretization of the phase space by utilizing a discrete number of particles called superparticles. Each superparticle represents a group of physical particles that are near each other in phase space. Mathematically, these superparticles are functions that satisfy the Vlasov equation. Each species in the system is represented by a superposition of computational particles, resulting in a discrete formulation of the distribution function in the Vlasov equation:

$$f_s(\vec{x}, \vec{v}, t) = \sum_p f_p(\vec{x}, \vec{v}, t) \tag{2.11}$$

where f_s represents the distribution function of the species s, whereas f_p denotes the distribution function of a computational particle. Since each simulation particle represents a group of real particles, it is necessary to adopt an appropriate spatial distribution of particles within the volume occupied by a superparticle. To this end, shape functions are employed, one for velocity and another for space. The selection of these shape functions is based on the twin goals of simplifying the computational problem and maintaining the physical consistency of the model.

$$f_p(\vec{x}, \vec{v}, t) = N_p S_x(\vec{x} - \vec{x}_p(t)) S_v(\vec{v} - \vec{v}_p(t)) \tag{2.12}$$

The shape function for velocity in almost all PIC codes is represented by a Dirac delta. This choice ensures that elements within a computational particle with the same velocity will remain close in phase space during the evolution of the system.

$$S_v(\vec{v} - \vec{v}_p(t)) = \delta(v_x - v_{xp})\delta(v_y - v_{yp})\delta(v_z - v_{zp}) \tag{2.13}$$

In all PIC codes, the position shape function typically used is the b-spline (**figure 2.1**), which refers to a series of consecutively higher-order functions obtained from each other through integration.
The first order b-splines named also flat-top function is defined as:

$$b_0(\xi) = \begin{cases} 1 & if \quad \xi < 1/2 \\ 0 & otherwise \end{cases} \tag{2.14}$$

The subsequent b-splines are obtained through integration as follows:

$$b_i(\xi) = \int_{-\infty}^{\infty} d\xi' b_0(\xi - x_i') b_{i-1}(\xi') \tag{2.15}$$

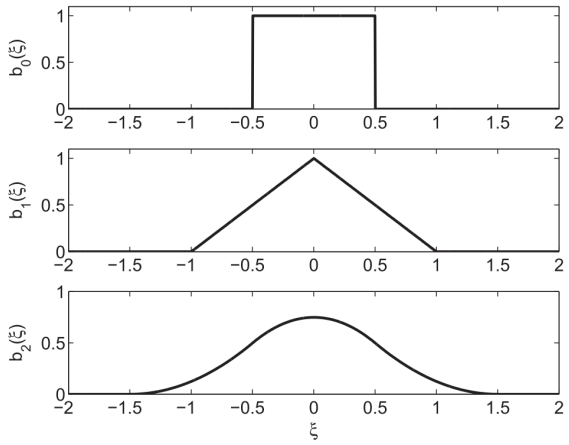

Figure 2.1: 0^{th}, 1^{st} and 2^{nd} order b-spline respectively [34].

Using the b-spline function the spatial functional shape of the computational particles is reported below:

$$S_x(\vec{x} - \vec{x}_p) = \frac{1}{\Delta x_p \Delta y_p \Delta z_p} b_i\left(\frac{x - x_p}{\Delta x_p}\right) b_i\left(\frac{y - y_p}{\Delta y_p}\right) b_i\left(\frac{z - z_p}{\Delta z_p}\right) \tag{2.16}$$

To obtain the explicit equation of motion in terms of position x_p and velocity v_p, it is necessary to calculate the moments of the Vlasov equation. The non-relativistic case is presented below using the formulation from reference [33], while the relativistic case can be found in reference [35]. The 0^{th} order moment, which is the same both for velocity and position, leads to the conservation of the number of physical particles per computational particle:

$$\frac{dN_p}{dt} = 0 \tag{2.17}$$

The first-order spatial moments instead lead to the definition of superparticles velocity:

$$\frac{d\vec{x}_p}{dt} = \vec{v}_p \tag{2.18}$$

While the velocity moments lead to the definition of acceleration considering Lorentz forces:

$$\frac{d\vec{v}_p}{dt} = \frac{q_s}{m_s}\left(\overrightarrow{E}_p + \vec{v}_p \times \overrightarrow{B}_p\right) \tag{2.19}$$

By obtaining the full set of moments up to the first order, the equation of motion for the computational particles in the simulation can be derived. These equations are analogous to Newton's equations of motion for regular particles, with the exception that the system of equations is discretized due to the presence of superparticles. The complete set of equations is reported below:

$$\begin{aligned} \frac{dN_p}{dt} &= 0 \\ \frac{d\vec{x}_p}{dt} &= \vec{v}_p \\ \frac{d\vec{v}_p}{dt} &= \frac{q_s}{m_s}\left(\overrightarrow{E}_p + \vec{v}_p \times \overrightarrow{B}_p\right) \end{aligned} \tag{2.20}$$

Where the Electric and Magnetic field for the computational particles are evaluated using the shape functions formulation:

$$\begin{aligned} \vec{E}_p &= \int S_{\vec{x}}(\vec{x} - \vec{x}_p)\vec{E}(\vec{x})d\vec{x} \\ \vec{B}_p &= \int S_{\vec{x}}(\vec{x} - \vec{x}_p)\vec{B}(\vec{x})d\vec{x} \end{aligned} \tag{2.21}$$

which requires the computation of the charge and current density:

$$\begin{aligned} \rho(\vec{x}, t) &= \sum_p q_s N_p S_{\vec{x}}(\vec{x} - \vec{x}_p) \\ \vec{j}(\vec{x}, t) &= \sum_p q_s N_p \vec{v}_p S_{\vec{x}}(\vec{x} - \vec{x}_p) \end{aligned} \tag{2.22}$$

It is important to remark that the equations derived are discretized by the superparticles, which introduces distortions in the phase space. This is mainly because the computational particles have a fixed shape, while an element in the phase space, accurately described initially by the shape functions, is distorted during the system evolution by the electric and magnetic fields. This leads to noises in the final results.

In order to numerically solve the system of differential equations **equation** (2.20), a time discretization method is required. The most commonly used method is the second-order accurate finite difference leapfrog scheme (shown in **figure 2.2**), where the position and velocity time steps are staggered by half a time step. The discretization scheme is presented below:

$$\begin{aligned}
&\frac{\vec{x}_p^{n+1} - \vec{x}_p^{n}}{\Delta t} = \vec{v}_p^{n+\frac{1}{2}} \\
&\frac{\vec{v}_p^{n+\frac{1}{2}} - \vec{v}_p^{n-\frac{1}{2}}}{\Delta t} = \frac{q_s}{m_s}\left[\overrightarrow{E}_p(x_p^n) + \left(\frac{\vec{v}_p^{n+\frac{1}{2}} + \vec{v}_p^{n-\frac{1}{2}}}{2}\right) \times \overrightarrow{B}_p(x_p^n)\right]
\end{aligned} \tag{2.23}$$

In this way, the evolution in time from n to $n+1$ of the x coordinate needs the velocity at the midpoint $n+1/2$, and the same is for velocity as shown in **equation** (2.23).

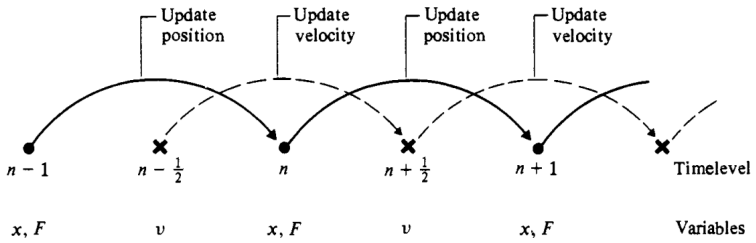

Figure 2.2: Illustrative representation of the leapfrog method [26].

In PIC codes, the procedure used to solve the equations of motion is commonly referred to as the particle pusher. In EPOCH, the particle pusher is utilized to solve **equation** (2.20) while considering relativistic effects, by implementing the Boris algorithm. This algorithm is a modified version of the leapfrog scheme, which is second-order accurate. The standard leapfrog scheme updates the position and velocity of particles using half-step displacement, while the electric and magnetic fields are evaluated at full steps. However, this introduces a phase error that grows linearly over time. The Boris algorithm corrects these errors by introducing an additional half-step displacement of particles between the electric and magnetic field evaluations. To calculate the particle trajectory, the electric and magnetic fields at half the timestep are used after being calculated from the Maxwell solver [29] (**section 2.2.3**). Furthermore, the acceleration is separated into two components: the acceleration in the electric field and the rotation around the magnetic field. The equations for the position and acceleration are provided below, but a detailed explanation of the Boris algorithm can be found in reference [36].

$$\begin{aligned}
&\frac{\vec{x}^{n+\frac{1}{2}} - \vec{x}^{n-\frac{1}{2}}}{\Delta t} = \frac{\vec{u}^n}{\gamma^n} \\
&m\frac{\vec{u}^{n+1} - \vec{u}^n}{\Delta t} = q\left(\overrightarrow{E}^{n+\frac{1}{2}} + \vec{v}^{n+\frac{1}{2}} \times \overrightarrow{B}^{n+\frac{1}{2}}\right)
\end{aligned} \tag{2.24}$$

Where γ is the Lorentz factor while $\vec{v}$ is an effective velocity:

$$\vec{u} = \gamma \vec{v} \qquad \gamma = \left[1 - \left(\frac{v}{c}\right)^2\right]^{-\frac{1}{2}} = \left[1 + \left(\frac{u}{c}\right)^2\right]^{\frac{1}{2}} \tag{2.25}$$

2.2.3 Space-Time discretization of Maxwell's equations

To solve Maxwell's equations (**equation** (2.6)) space and time discretization are needed. In PIC codes different discretization schemes can be used. In EPOCH it is used the *Yee-FDTD* (Finite difference time domain) scheme. In particular, a modified version of the *leapfrog* scheme, described in **section 2.2.2** for the particle pusher, is used to discretize the time domain. In particular, the electric field is updated using the curl of the magnetic field at the previous time step, while the magnetic field is updated using the curl of the electric field at the current time step:

$$\begin{aligned} \overrightarrow{E}^{n+\frac{1}{2}} &= \vec{E}^n + \frac{\Delta t}{2}\left(c^2 \nabla \times \vec{B}^n - \frac{\vec{J}^n}{\epsilon_0}\right) \\ \overrightarrow{B}^{n+\frac{1}{2}} &= \overrightarrow{B}^n - \frac{\Delta t}{2}\left(\nabla \times \vec{E}^{n+\frac{1}{2}}\right) \end{aligned} \tag{2.26}$$

The current is subsequently updated to J^{n+1} by the particle pusher, and the fields are updated from $n + \frac{1}{2}$ to $n + 1$:

$$\begin{aligned} \overrightarrow{B}^{n+1} &= \vec{B}^{n+\frac{1}{2}} - \frac{\Delta t}{2}\left(\nabla \times \vec{E}^{n+\frac{1}{2}}\right) \\ \overrightarrow{E}^{n+1} &= \overrightarrow{E}^{n+\frac{1}{2}} + \frac{\Delta t}{2}\left(c^2 \nabla \times \vec{B}^{n+1} - \frac{\vec{J}^{n+1}}{\epsilon_0}\right) \end{aligned} \tag{2.27}$$

The discretization of time alone is not sufficient to solve the set of equations, therefore a spatial discretization must also be considered. To achieve this, a second-order accurate central difference scheme is applied to staggered grids for each electric and magnetic vector field component. Specifically, the electric fields are located at the cell faces, while the magnetic fields are located at the cell edges (**figure 2.3**). This approach is known as the Yee staggered grid [37], which ensures that $\overrightarrow{E}$ and $\overrightarrow{B}$ are perpendicular and the curl operation is naturally satisfied (**equation** (2.6)).[34] Furthermore, the conservation of the divergence of $\overrightarrow{B}$ is also maintained. In this way, all spatial derivatives in **equation** (2.20) are expressed as follows [29]:

$$\left(\frac{\delta E_y}{\delta x}\right)_{i,j,k} = \frac{E_{y_{i+1,j,k}} - E_{y_{i,j,k}}}{\Delta x} \tag{2.28}$$

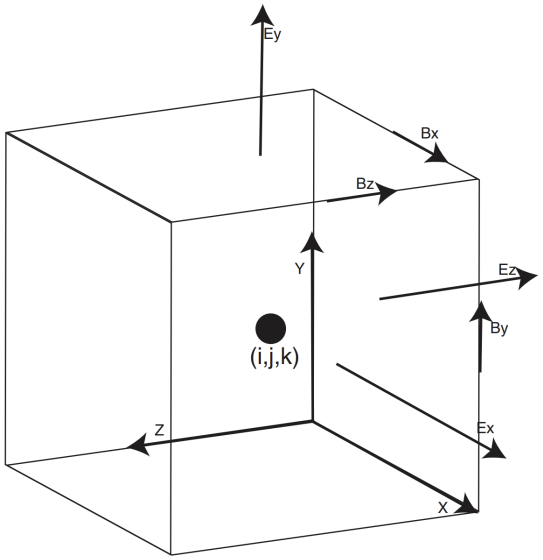

Figure 2.3: Yee staggered grid. [29]

To solve the discretized Maxwell's equations (**equation** (2.26) and **equation** (2.27)), it is necessary to obtain the current and charge density onto the grid. This is achieved through the *current deposition scheme* proposed by Esirkepov [38], which is used to deposit the current and charge density onto the grid while conserving charge and momentum. The fundamental concept is to interpolate the current and charge carried by each macroparticle onto the grid using a weighted scheme that considers the flux of charge passing through cell boundaries:

$$(J_k)^{n+1}_{i+1,j,k} - (J_k)^{n+1}_{i-1,j,k} = -q_s \frac{dx}{dt} (W_k)^{n+1}_{i,j,k} \tag{2.29}$$

Where k subscript represents the coordinate x, y or z, while W is the weight which is typically such that it satisfies the conservation of charge and current, and it depends on the particle distribution and the simulation grid. Once the current density is known Maxwell solver can be initialised, the charge density is redundant and it is used for diagnostic reasons.

2.3 Epoch software

The equation described in **section 2.2**, which are the core of a PIC code, are solved in EPOCH code by a computational cycle which follows the steps listed below:

1. Particle Pusher (described in **section 2.2.2**): This step calculates the new position and velocity of each particle in the simulation based on the electric and magnetic fields at the previous time step. The electric and magnetic fields are taken from the initialisation conditions at the first step.

2. Maxwell Solver (described in **section 2.2.3**): This step calculates the electric and magnetic fields at the current time step based on the charge and current densities obtained from the particles.

3. Current Deposition (described at the end of **section 2.2.3**): This step updates the currents on the grid based on the motion of the particles.

4. Repeat the above steps until the simulation is complete.

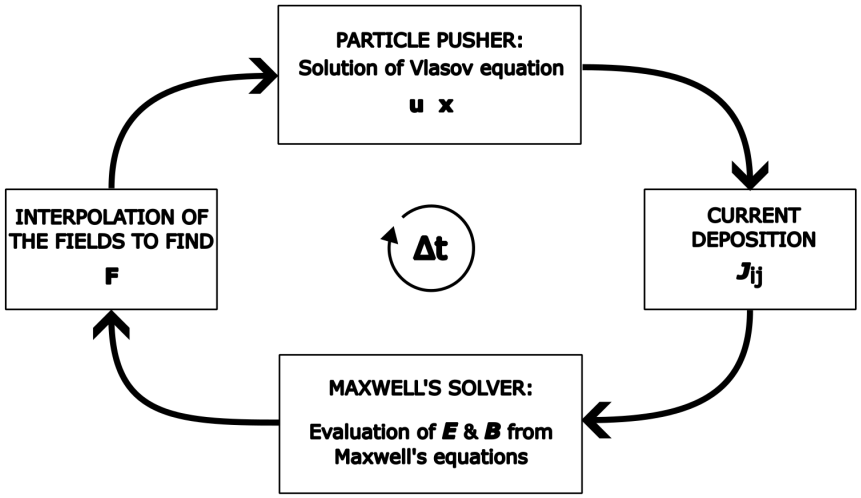

Figure 2.4: Illustration of a PIC computational cycle

The EPOCH code includes all the features of a standard PIC code, but it also incorporates additional extensions to account for collisions, ionization, and QED effects.

As mentioned previously, PIC codes are commonly used for simulating collisionless systems, where particle interactions over short ranges are neglected. At high temperatures and low densities, the effects of collisions can typically be disregarded without introducing any distortion in the physics. However, at low temperatures and

high densities, collisional effects become more significant and cannot be neglected. A laser-induced plasma system is initialised at room temperature and subsequently, after being irradiated by the laser, it reaches the temperature of a laboratory plasma. The electron population in this system is temporarily far from equilibrium due to the large temperature gradient. In such conditions, both kinetic and collisional effects must be considered. [29, 39]

In order to account for particles collisions, PIC codes utilize a collision algorithm that scatters particles stochastically in phase space. In EPOCH, two types of algorithms have been introduced: one based on the model presented by Sentoku and Kemp [40], and the other based on the model by Nambu-Pérez [41]. The algorithm proposed by Sentoku and Kemp takes relativistic effects into consideration and is based on a Monte Carlo approach. It is designed to handle collisions between highly charged ions and neutral gas, which can result in significant energy loss and ionization. In the Monte Carlo approach, the probability of collision and ionization is sampled at each time step, and the particle properties are updated accordingly. [40] Similarly to the previous algorithm, the algorithm proposed by Nambu and then improved by Perez also considers relativistic effects and updates particle properties using Monte Carlo sampling of the cross-section. [41]

Certainly, it is important to consider ionization, which can have significant macroscopic consequences, such as laser defocusing [29]. As explained in **section 1.4.2**, there are different modes by which electrons can ionize, and EPOCH includes models to take into account the most relevant ionization phenomena. Mainly two types of ionization models are considered: field ionization and collisional ionization. Moreover, field ionization can divided into multiphoton ionization and tunnelling ionization , as stated in **section 1.4.2**.

The field ionization process is modelled in EPOCH using the ADK model proposed in [42], which is a special case of the WKB model [43]. In addition to this, Barrier Suppression Ionization (BSI) is a specific case of tunnelling ionization that occurs when the potential energy barrier is lowered below the electron binding energy, allowing the electrons to escape according to classical physics laws. In situations where the plasma is collisional, another type of ionization process must be considered: collisional ionization. EPOCH includes a module that takes into account ionization by electron impact on a bounded electron, followed by ionization. Due to the unavailability of electron impact ionization cross-sectional data for many elements, the module uses the MBELL equation [44] for $q \leq 36$ and the relativistic modified Bethe model for $q > 36$ to approximate the cross-section. Here, q is defined as $q = Z - N_{nl}$, where Z is the atomic number and N_{nl} is the total number of electrons in all sub-orbitals up to the ionizing orbital. [29]

With the increase in laser power, which can reach up to 10 PW, the relevance of QED effects must be considered in PIC models that aim to simulate the interaction between lasers and matter accurately. The η parameter can be used to quantify

the importance of QED effects:

$$\eta = \frac{e\hbar}{m_e^3 c^4} \left| F_{\mu v} p^v \right| = \frac{E_{RF}}{E_s} \tag{2.30}$$

Where E_{rf} is the electric field in the rest frame of the electron and E_s is the critical field for QED, which is $1.3 \cdot 10^{18}, \mathrm{V/m}$. When $\eta \gtrsim 0.1$, which corresponds to a laser intensity of $5 \times 10^{22}\,\mathrm{W/cm^2}$, QED effects become relevant. To account for these stochastic effects, EPOCH uses a Monte Carlo algorithm to solve the equations of motion, considering stochastic γ emission and treating the motion between emission events classically. This can be done thanks to the weak-field assumption for which the laser fields are much weaker than the Schwinger field [45]. The code tracks the trajectory of each particle, and at each step, it calculates the probability of photon emission or pair production based on the local electromagnetic field. If a photon or pair is emitted, the code calculates the kinematics of the process, including the energy and direction of the emitted particles. The Monte Carlo emission algorithm is fully described in reference [46] and summarized in [45].

Chapter 3

Model Validation: Replicating Reference Results

This chapter is dedicated to simulations conducted using the EPOCH PIC software. Specifically, it focuses on a benchmarking case study involving a cutting-edge paper on the EPOCH software ([29]). The article describes the program's features and tests specific scenarios to verify its reliability. This verification involves comparing the results obtained through the simulation with theoretical studies and simulations conducted using other software types.

3.1 Self heating mechanism in plasma simulation through PIC-codes

The first simulation focuses on a phenomenon encountered in all PIC codes known as self-heating, a non-physical heating of the plasma induced by numerical simulations, also referred to as numerical heating. **Chapter 2** discussed the numerical methods employed to model the behavior of charged particles in electromagnetic fields. However, these methods can sometimes introduce artificial effects, including numerical heating. Numerical heating arises due to aliasing modes in the electromagnetic field, leading to undesired outcomes in PIC simulations. Nevertheless, this effect can be managed and mitigated by carefully selecting suitable numerical parameters for the simulation, such as lower resolution (cell dimensions) than the Debye length or using higher-order shape functions.

The EPOCH simulation conducted considers a solid density plasma with $n_e = n_{23} = 1 \times 10^{23}\,\mathrm{cm}^{-3}$ (equivalent to 100 times the critical density n_c) and an initial

temperature of 1 keV. Different spatial domains have been explored to assess their impact on self-heating mechanisms. Additionally, the number of particles per cell has been varied for comparison. **Figure 3.1a** depicts plasma self-heating with a resolution $\Delta x = 1.5c/\omega_p$ using 16 particles per cell. Specifically, the figure illustrates energy conservation for the total particle kinetic energy E. The cell width is determined based on the plasma frequency, which in turn relies on the electron density (**equation** (1.4)). The x-axis indicates the percentage variation in energy relative to the initial energy, the variation is due to self-heating given the absence of a heat source in the simulation. As shown in **figure 3.1a**, the percentage variation in energy is well above 100% of E_0. To alleviate self-heating, current smoothing has been introduced along with the same initial conditions as before (**figure 3.1b**). This approach diminishes self-heating, resulting in an energy increase of around 100%. Current smoothing involves applying a smoothing function to the current generated during particle pushes. This technique aids in reducing noise and self-heating.

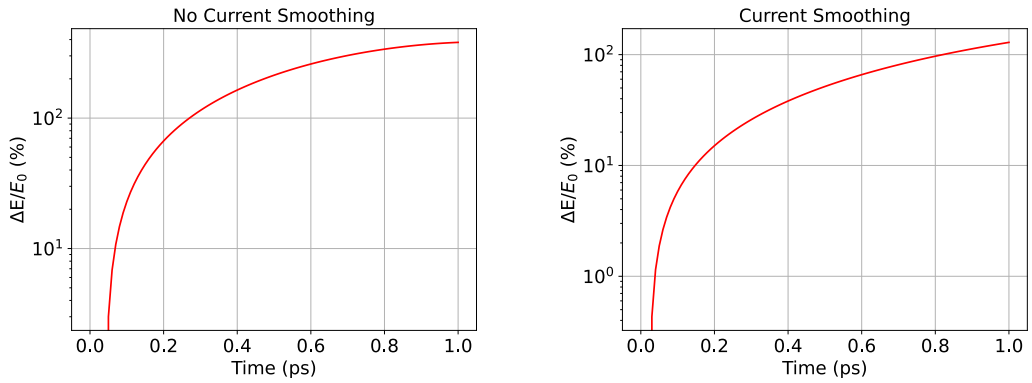

Figure 3.1: Temporal progression of self-heating mechanisms. In Panel **a**, the outcome of a simulation is presented, conducted with a spatial resolution of $\Delta x = 1.5c/\omega_p$ and 16 particles per cell (ppc). Meanwhile, Panel **b** showcases the results of another simulation carried out using the same spatial resolution of $\Delta x = 1.5c/\omega_p$ and 16 ppc, yet with the inclusion of current smoothing.

By adjusting the resolution and increasing the particle count per cell, a potential reduction in this phenomenon is anticipated. Specifically, a simulation was conducted utilizing a cell dimension of $1.5c/\omega_p$ and 64 particles per cell the results of which are showcased by the blue curve in **figure 3.2a**, along with a simulation executed with $\Delta x = 0.5c/\omega_p$ and 16 particles per cell depicted in green. **Figure 3.2a** provides insight into how augmenting the particle count per cell correlates with diminished self-heating, manifesting as a peak reduction of around

10% (represented by the blue curve). The same holds for the other simulation in which the dimension of the cell has been reduced.

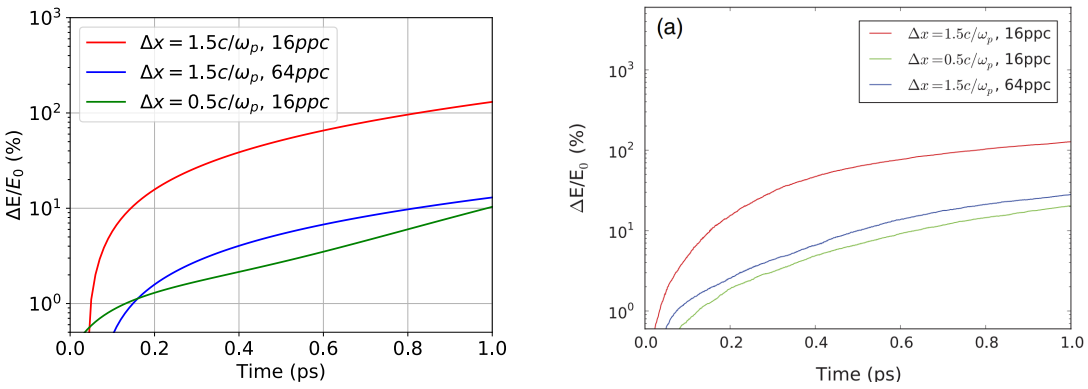

(a) **(b)**

Figure 3.2: Panel **(a)**: illustration of the self-heating mechanism across various simulations, showcasing how this phenomenon is affected by the main simulation parameters: resolution and the number of particles per cell. A general guideline emerges, indicating that increasing the number of particles per cell and decreasing resolution results in a reduction of self-heating effects. Panel **(b)**: results obtained in the reference paper.

In **figure 3.2b** it is reported the result obtained in the reference article. The result obtained are almost equal to the original, the difference in the behaviour of the green curve in **figure 3.2a** is due to the applied smoothing function.

3.2 Thermalization of non-equilibrium distribution via self-collisions

Subsequently, a simulation was conducted as per reference [29] to assess the EPOCH collision operator's performance. The aim was to confirm whether an initially non-equilibrium electron distribution would eventually reach thermal equilibrium, attaining a Maxwellian distribution as required by the H-theorem. The simulation has been initialized with a constant distribution characterized by a momentum magnitude $p = p_c$ with $p_c = 6.04 \times 10^{-24}\,\mathrm{kg\,m\,s^{-1}}$. If the collision operator works correctly this distribution should then thermalize into a Maxwellian distribution, maintaining the same average energy evaluated as $T = p_c^2/(5m_eK_b)$, within a timeframe equivalent to the collisional time $t_c = (\epsilon_0\pi m_e^2 v_{te}^3)/(e^4 n_e log(\Lambda))$ which has been employed as the simulation duration. The simulation has been initialized with an electron density of $n_e = 1 \times 10^{30}\,\mathrm{m^{-3}}$, a spatial resolution of $\Delta x = \lambda_d$ with 4 cells along the x-direction, and a Coulomb logarithm ($log(\Lambda) = 4$). To minimize noise, 2048 particles per cell were used for this simulation; this number could be augmented for noise reduction. Notably, the simulation outcomes replicate those obtained in reference [29], whereby the initial distribution eventually evolves into a Maxwellian even though certain parameters slightly deviate from those employed in the reference study (**figure 3.3c**).

3.3 Relaxation of an anisotropic particle distribution

A simulation on temperature isotropization has been carried on in reference [29] to test the angular scattering properties of the collision operator. The initial condition was set with an anisotropic temperature distribution, and the aim was to verify if collisions would lead to its isotropization. The system has been initialized using an electrons distribution that is a product of three Maxwellians with temperatures $T_x = 100$ eV, $T_y = T_z = 10$ eV:

$$\begin{aligned} f(p_x, p_y, p_z) = &\left(\frac{m_e}{2\pi K_b T_x}\right)^{\left(\frac{1}{2}\right)} \left(e^{\frac{-p_x^2}{2K_b m_e T_x}}\right) \cdot \\ &\cdot \left(\frac{m_e}{2\pi K_b T_y}\right)^{\left(\frac{1}{2}\right)} \left(e^{\frac{-p_y^2}{2K_b m_e T_y}}\right) \cdot \\ &\cdot \left(\frac{m_e}{2\pi K_b T_z}\right)^{\left(\frac{1}{2}\right)} \left(e^{\frac{-p_z^2}{2K_b m_e T_z}}\right) \end{aligned} \tag{3.1}$$

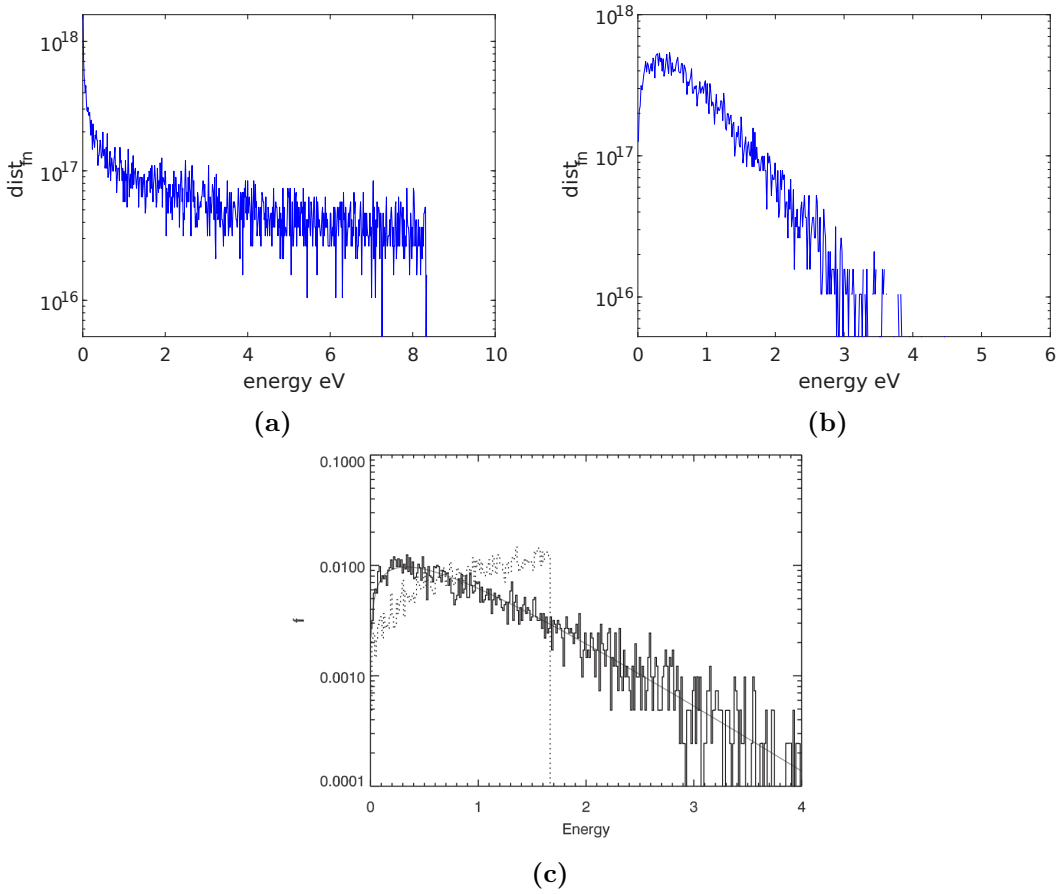

Figure 3.3: Top: Energy distribution function of particles within the system. Panel **(a)** depicts the initial energy distribution, while panel **(b)** illustrates the final distribution of thermally equilibrated particles, which follows a Maxwellian distribution. Bottom: result obtained in the reference article.

The ions are assumed to be at rest, and electron-electron collisions are disregarded. The initial electron density was set to $1 \times 10^{27}\,\mathrm{m}^{-3}$. For each spatial dimension (x, y, and z), four cells were considered, each with a particle count of 500. In **figure 3.4a**, the initial velocity distribution is presented as a function of the angle θ, where $\tan(\theta) = v_y/v_x$, at the simulation's outset. Notably, as depicted in **figure 3.4a**, the peak anisotropy occurs around $\theta = 0 + k\pi$. On the other hand, **figure 3.4b** illustrates the distribution's temporal evolution. It is apparent that the distribution relaxes over time; however, a considerable amount of noise is present. This noise primarily arises due to the limited number of cells and particles used in the simulation. While increasing the number of cells and particles could mitigate this noise, such an adjustment would demand a significant increase in

computational time, which was deemed impractical for this study. The bottom part of **figure 3.4** represents the results obtained in the reference article divided in different energy bands. It is evident that, from a physical perspective, the results are comparable, even thought distinct energy bands were not taken into account in the current simulation.

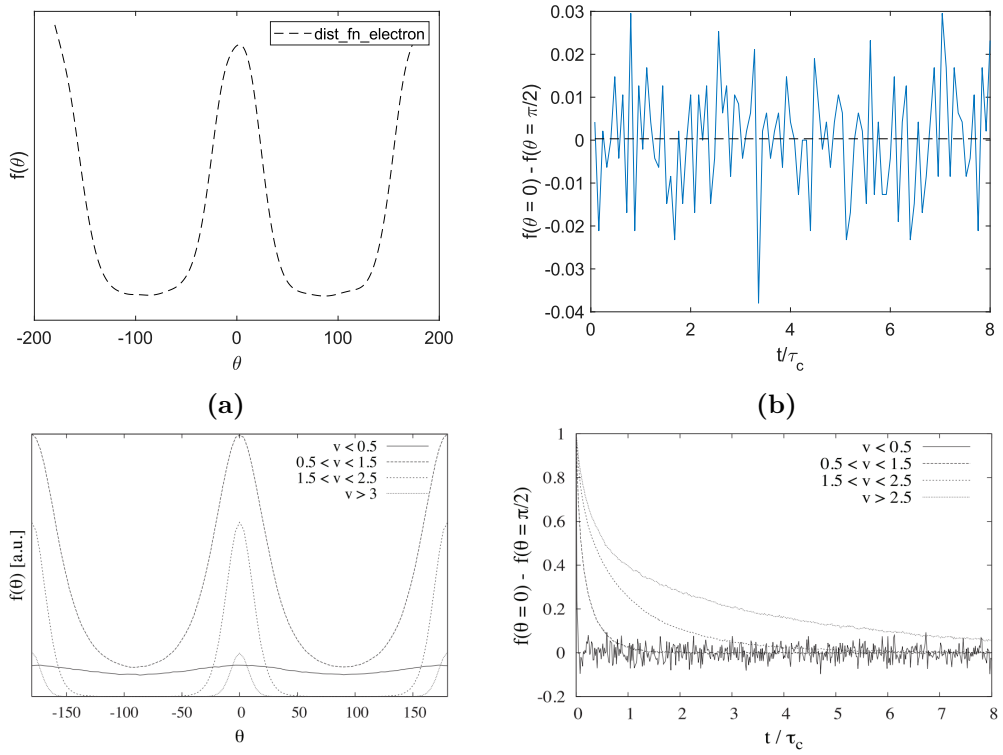

Figure 3.4: Top: particle distribution obtained throughout the simulation. Panel **a** presents the initial anisotropic particles distribution in function of the angle θ. Meanwhile, panel **b** illustrates the temporal evolution of the distribution, indicating its rapid relaxation attributed to collisions. Bottom: results obtained in the reference paper for different energy bands.

3.4 Collisional ionisation of carbon

Another simulation has been conducted to investigate the collisional ionization of a carbon plasma. The simulation was initiated by considering a preformed plasma consisting of C+1 ions and electrons, both having a solid density of $n_i = n_e = 1 \times 10^{29}\,\mathrm{m}^{-3}$, ensuring charge neutrality. The spatial variation in density, as well as the initial temperature, are described in the following system of equations (**equation** (3.2) and **equation** (3.3)), as they are piecewise constant as defined in reference [29].

$$\rho(x) = \begin{cases} 0 & x \leq 0 \\ \rho_{max}(520x - 100) & 0.2 < x < 0.25 \\ 30\rho_{max} & 0.25 \leq x < 0.7 \\ 0 & 0.7 \leq x \end{cases} \tag{3.2}$$

$$T_e(x) = \begin{cases} T_{min} & x \leq 0.2 \\ (T_{max} - T_{min})\frac{0.5-x}{0.3} + T_{min} & 0.2 < x < 0.5 \\ T_{min} & 0.5 \leq x \end{cases} \tag{3.3}$$

In the systems above, $\rho_{max} = 1 \times 10^{28}\,\mathrm{m}^{-3}$, $T_{min} = 15\,\mathrm{eV}$ and $T_{max} = 600\,\mathrm{eV}$ while the x coordinates are expressed in µm. The systems of equations are graphically shown in the figures below (**figure 3.5**).

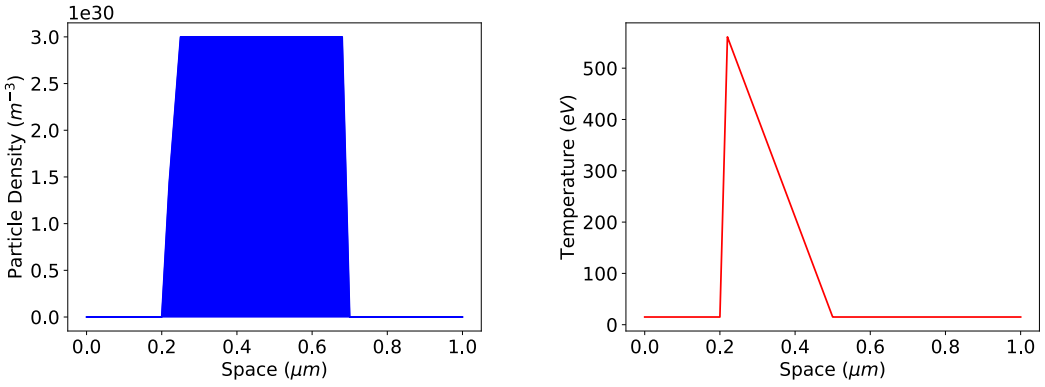

(a) **(b)**

Figure 3.5: In panel **(a)** it is shown the density variation in space which represents the carbon plasma at the beginning of the simulation. In panel **(b)** it is reported the electron temperature at the beginning of the simulation; the carbon temperature is constant and equal to 15 eV.

Subsequently, the carbon plasma was exposed to a laser with an intensity of $1 \times 10^{16}\,\mathrm{W\,cm^{-2}}$, a duration of 350 fs, and a wavelength of 0.25 µm. The laser's time profile was set to "auto", utilizing a Gaussian profile within the laser's time interval. The laser's characteristics are crucial because excessively high intensity and duration could lead to the immediate and complete ionization of carbon up to level 6. This, in turn, would hinder the investigation of collisional ionization behavior, which becomes significant after the laser pulse. The interaction with the laser rapidly ionizes the C+1 ions, causing them to promptly reach the 4th ionization state through field ionization and, in particular, multiphoton ionization, as barrier suppression ionization only becomes meaningful at higher laser intensities, and thus, it was deactivated.

The graph below (**figure 3.6**) illustrates the evolution of the average ionization state over time. It can be observed that carbon, starting from a charge of +1, is ionized to +4 within a short time. At this point, an exchange of energy between electrons and ions is expected, leading to collisional ionization, which further ionizes the carbon ions up to a charge of +6. However, in the simulation, carbon ionization ceases at a charge of +4. This might be due to the fact that the electron energy may be insufficient to further ionize the carbon +4 ions. The increase in charge mirrors the original simulation conducted in the referenced article, though with fewer output files generated in this case, resulting in a less steep peak increase. The reduction in output files was necessitated by time constraints, as the simulation time is considerably longer.

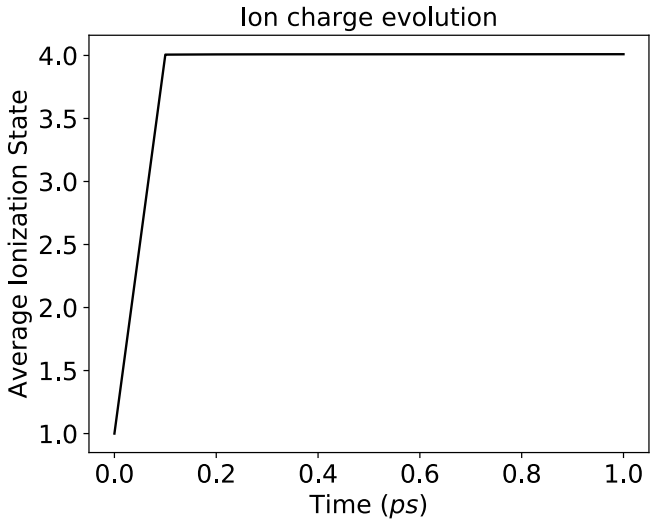

Figure 3.6: Evolution of the mean carbon charge in the system. The simulation is initiated with a carbon charge of +1 which evolves, thanks to the laser field ionization, up to charge +4.

The evolution of all carbon ions over time is depicted in **figure 3.7**, highlighting how the initial carbon +1 ions are almost entirely converted into C4+. The presence of other carbon species is negligible.

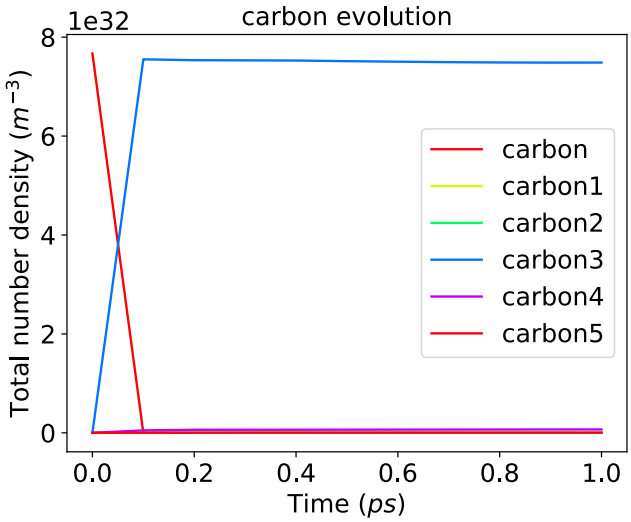

Figure 3.7: Changes in carbon ion states over time. It is evident that carbon ions initially at the +1 charge state are rapidly ionized to reach a +4 charge state. The amount of other ions is negligible.

The evolution of electron and carbon temperatures is presented below, revealing an anomalous temperature behavior where the carbon temperature surpasses the electron temperature. Ideally, the carbon temperature should remain low and nearly identical to the initial temperature throughout the simulation. This anomaly may explain why carbon ionization by collision with electrons is not observed. Further simulations were conducted to explore the same phenomenon while varying different parameters. However, all these simulations exhibited the same behavior, with no observable ionization by collision in any of them.

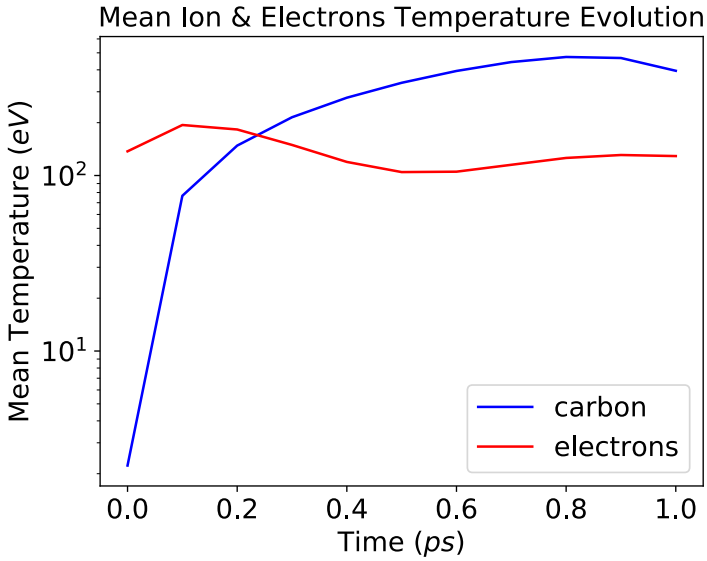

Figure 3.8: The figure presents the time-dependent temperature evolution of electrons and ions on a semilogarithmic graph along the y-axis. the temperature of carbon atoms exceeds that of electrons after 0.25 ps resulting in a non-physical behaviour of the system.

Chapter 4

Exploring Target Variations for Plasma Generation

This chapter presents simulations that focus on the interaction between lasers and different materials. These simulations were conducted to enhance the comprehension of how lasers interact with matter. The study specifically explored the effects of varying materials and laser intensities on the evolution of ions and temperatures within the system. Additionally, simulations were performed to investigate plasma formation for proton-boron fusion, utilizing a particular target setup. In this configuration, the primary target, known as the "pitcher", is exposed to a laser beam, resulting in rapid ionization and plasma formation. Subsequently, the laser's energy accelerates light nuclei, such as protons, which then engage with a secondary target composed of boron to initiate proton-boron-11 fusion. It is noteworthy that all simulations conducted in this study employ a one-dimensional approach. This decision was motivated by the desire to reduce computational time, which can be substantial in Particle-in-Cell (PIC) simulations of these experiments. Furthermore, a one-dimensional framework proves sufficient for characterizing the interaction and evaluating the properties of the generated plasma.

4.1 Aluminum target

The initial simulation involves an aluminum foil target with a thickness of 4 µm and an initial temperature of 293 K. The simulation has been configured with 500 cells and 500 particles per cell. The cell dimensions were carefully selected to ensure they remained smaller than the Debye length λ_d (**section 1.1**). The target is exposed to a laser beam with the following parameters: intensity I_{max} of 1×10^{16} W cm^{-2}, wavelength of 0.25 µm, and pulse duration of 100 fs. The system's evolution is tracked for a duration of 500 fs within a spatial domain of 16 µm. During this brief pulse, the primary ionization mechanisms are attributed to the laser field and to photon-ionization. Consequently, only field and multiphoton ionization processes are activated. The initial conditions are visualized in **figure 4.1**, providing a snapshot of the density and temperature at the simulation's outset. The particle density associated with the solid target was evaluated considering the atom's density, the atomic mass and Avogadro's number.

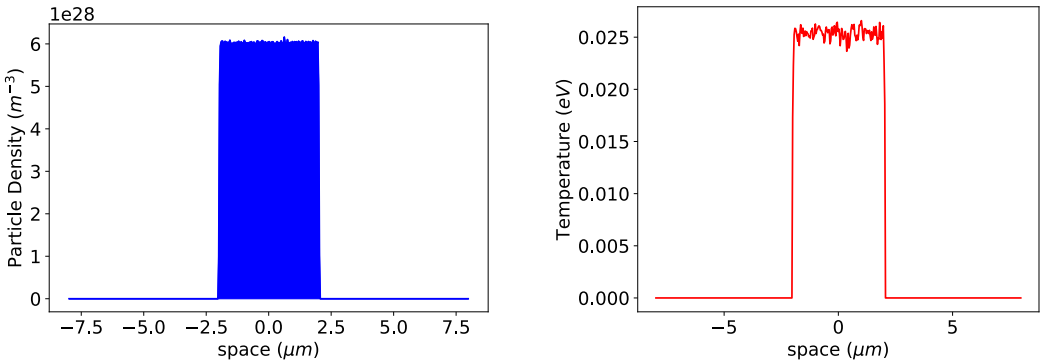

(a) **(b)**

Figure 4.1: Initial conditions. In panel **(a)**, the density associated with the solid aluminum foil is presented. Panel **(b)**, on the other hand, displays the initial temperature within the system.

The laser starts interacting with the target after 10 fs, leading to prompt ionization of the aluminum target, resulting in Aluminum ions. Before the end of the 110 fs laser pulse, the target is completely ionized up to charge +13. This behavior is depicted in **figure 4.2**, which illustrates the evolution of the mean charge in the system. The sharp increase in the curve represents the prompt ionization of the target. Furthermore, it can be observed that complete ionization of the aluminum occurs before 0.11 ps, which marks the end of the laser pulse. At this point, the plasma is composed only of Aluminum ions and free electrons.

Once the target is ionized, its temperature increases, especially the electron

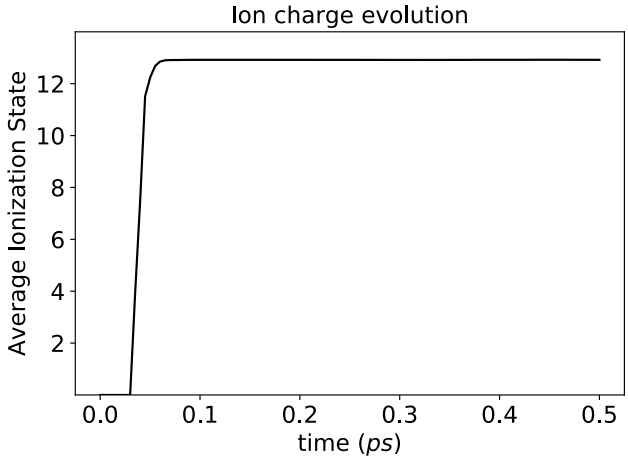

Figure 4.2: Evolution of the mean charge throughout the simulation. Notably, there is a rapid surge in the mean charge, culminating at +13. Consequently, after less than 0.1ps the plasma comprises solely of Aluminum ions and freely moving electrons within the spatial domain.

temperature since electrons absorb most of the laser energy in the first few femtoseconds. The temperature evolution for both electrons and ions, expressed in eV, is shown in **figure 4.3**. The graph uses a semi-logarithmic scale along the y-axis. The maximum temperature reached by the electrons is approximately 10 MeV, which also serves as a measure of their kinetic energy. The difference between the two temperatures is approximately two orders of magnitude. Furthermore, the ions temperature increases with less sharpness. This is mainly because the laser interacts with the electrons through field ionization, leading to Aluminum ionization. Moreover, the generated ions are heavier than the electrons, resulting in less effective energy transfer during collisions between the two species.

During the interaction, the temperature increase leads to plasma expansion in space, reducing local density. This behavior is illustrated in **figure 4.4**.

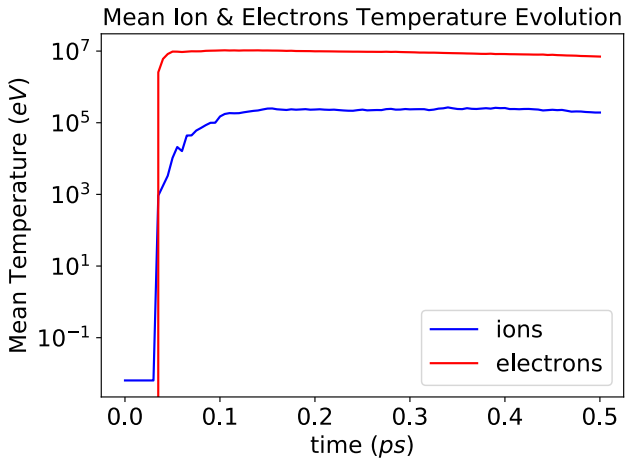

Figure 4.3: Temporal evolution of ion (blue) and electron (red) temperatures. Notably, electron temperatures rise more rapidly than ion temperatures due to the initial laser interaction with electrons within the first few femtoseconds of the simulation.

4.2 Cesium Target

The second simulation involves a cesium target with a thickness of 4 µm and a temperature of 293 K. Boundary conditions for this simulation consist of a laser on the left side, as it is attached to the laser, and an open boundary on the right side. This open boundary permits particle expansion in space and energy loss from the system after a certain duration. The primary objective of the simulation is to study the interaction with the laser and the characteristics of the generated plasma. The laser parameters used in this simulation are identical to the previous case. The system's evolution is tracked for 500 fs within a spatial domain of 16 µm. Only multiphoton and field ionization mechanisms are activated as the primary ionization processes since they are most significant. The system features 500 cells and 500 particles per cell. Density was calculated similarly to the aluminum target, and initial conditions regarding temperature and density are presented in **figure 4.5**.

Under these conditions, the cesium target remains mostly un-ionized. Only a small fraction of cesium atoms becomes ionized due to laser interaction. The target remains nearly solid by the simulation's conclusion, with a slight reduction in cesium density. **Figure 4.6** demonstrates this, along with ion charge evolution, which exhibits an average charge of about 0.3 within the system post-laser interaction. This indicates that a significant portion of the initial cesium remains un-ionized.

Since the target remained non ionized under the previously described conditions, an additional simulation was carried out. This simulation employed a laser intensity of $1 \times 10^{20}\,\mathrm{W\,cm^{-2}}$, maintaining all other initial conditions unchanged.

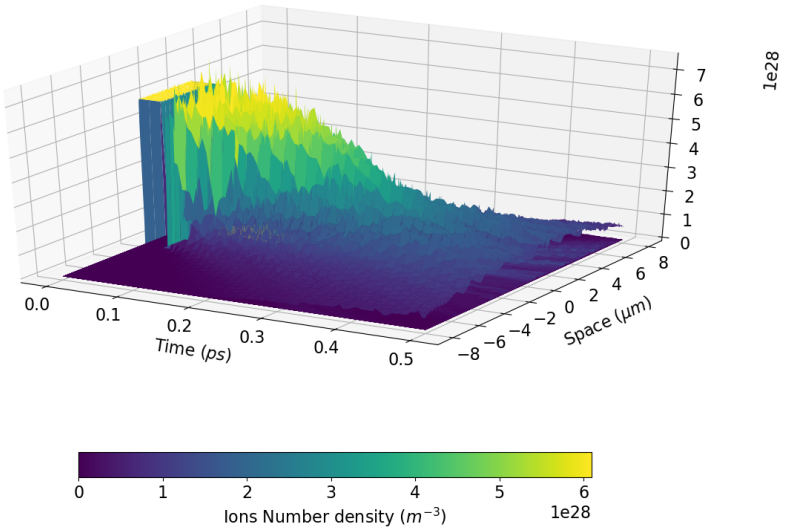

(a)

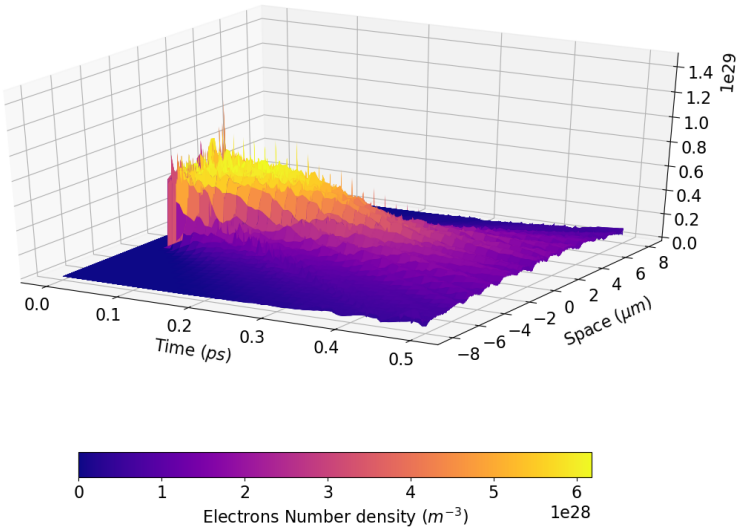

(b)

Figure 4.4: Spatial and temporal evolution of ions **(a)** and electron density **(b)** for the Aluminum target. The left side of each graph displays the initial condition, featuring a solid target with an absence of electrons in the system. As time progresses, one can observe the transformation in density, the spatial expansion of the plasma, and the emergence of electrons.

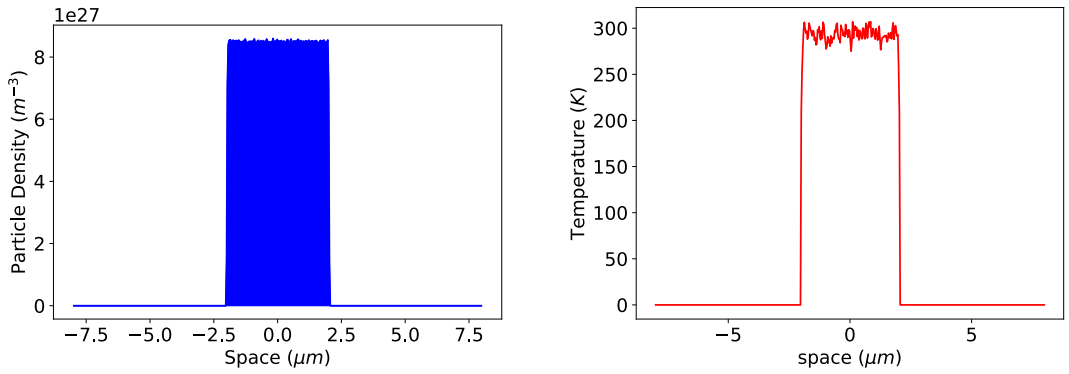

(a) **(b)**

Figure 4.5: Simulation initial conditions. In panel **(a)** it is reported the target density while in panel **(b)** its temperature.

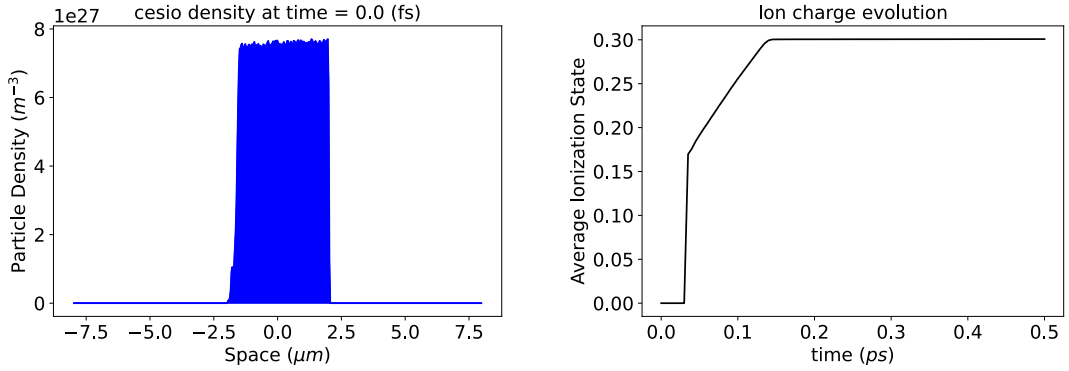

(a) **(b)**

Figure 4.6: Simulation outcome in terms of density and ion charge evolution. In panel **(a)** it is shown the density at the end of the simulation 500 fs, while in panel **(b)** the evolution of the average ionization state.

This simulation exhibited a different behavior, with the target becoming ionized and forming a plasma. However, even after 500 fs, a portion of the initial cesium remains un-ionized, as demonstrated in **figure 4.7**, alongside ion charge evolution showing an average charge of about 40 within the system post-laser interaction.

Initially, the laser interacts with electrons, heating them to temperatures in the order of 1×10^9 eV, as shown in **figure 4.8**, along with the cesium ions' temperature, which increases upon field ionization. However, the ions' temperature remains significantly lower than the electron temperature by approximately two orders of magnitude. Density evolution in space and time for both electrons and ions is similar

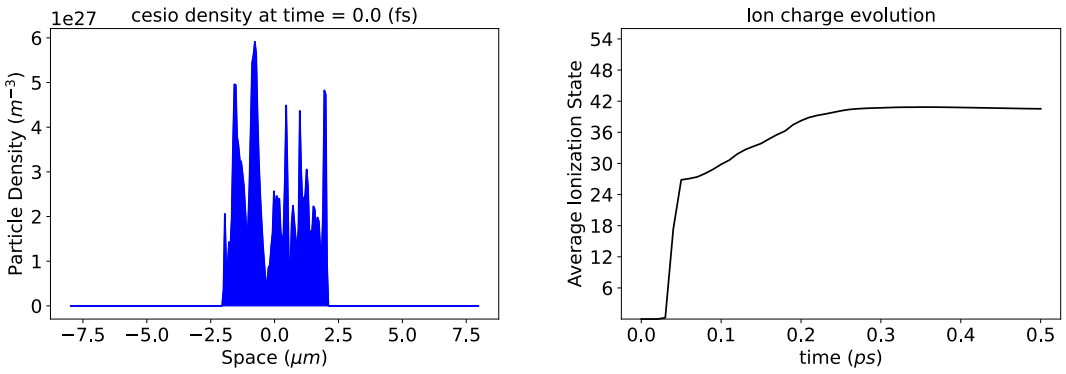

(a) **(b)**

Figure 4.7: Outcome of the simulation with a maximum laser intensity of $1 \times 10^{20}\,\mathrm{W\,cm^{-2}}$. On the left side there is the density at the final time frame 500 fs, while on the right side the ion charge evolution.

to the previous simulation, showing the plasma's spatial expansion (**figure 4.9**).

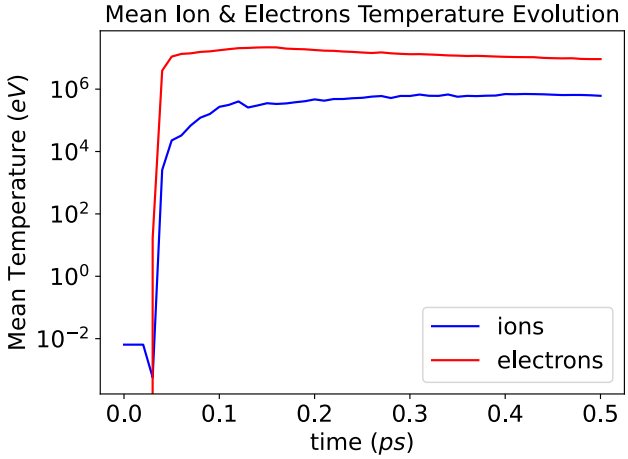

Figure 4.8: Temperature evolution for electrons and ions for the cesium target subjected to a laser intensity of $1 \times 10^{20}\,\mathrm{W\,cm^{-2}}$.

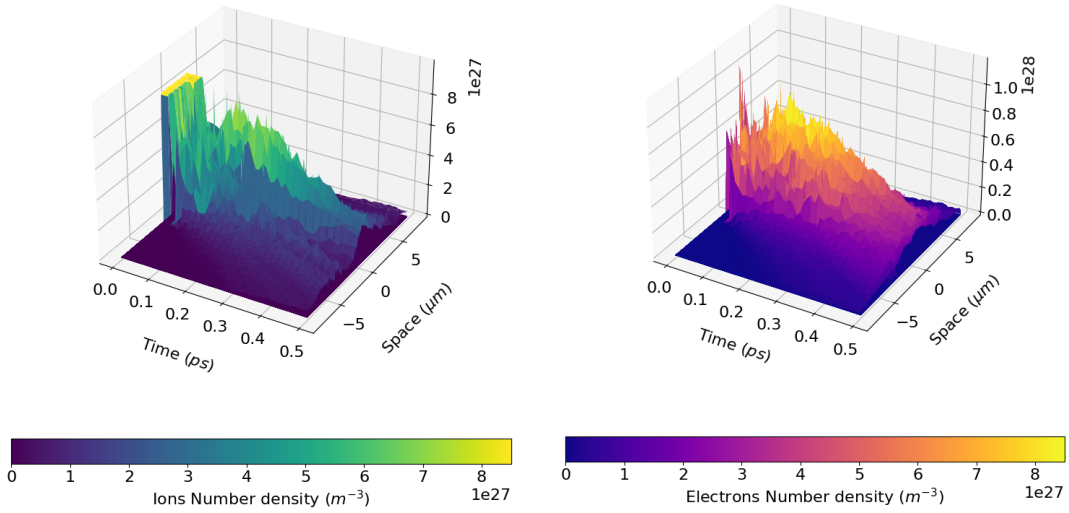

(a) **(b)**

Figure 4.9: Spatial and temporal evolution of ions (a) and electron density (b) for the cesium target subjected to a laser intensity of $1 \times 10^{20}\,\mathrm{W\,cm^{-2}}$.

4.3 Lead Target

The simulation featuring a Lead target employs a lead material with the same initial conditions as the previous simulation, for both the laser $I_{max} = 1 \times 10^{16}\,\mathrm{W\,cm^{-2}}$ and target. The results indicate rapid ionization of the lead wall with a laser intensity of $1 \times 10^{16}\,\mathrm{W\,cm^{-2}}$, eliminating the need for further intensity increases, which was necessary for cesium. **Figure 4.10** shows the average charge within the system, reaching approximately 64 at the end of the simulation. The charge's increase is not as rapid as observed with the lighter nuclei in the previous simulations; it is rapid up to 40, after which the curve's slope reduces as additional ionization of ions requires more energy. The electron temperature in this case is higher with respect to the cesium target irradiated by a laser with $I_{max} = 1 \times 10^{20}\,\mathrm{W\,cm^{-2}}$, reaching approximately 100 MeV, while the ions maintain a temperature of 1 MeV (**figure 4.11**). The density evolution for both electrons and ions in space and time mirrors previous simulations, with the plasma expanding spatially.

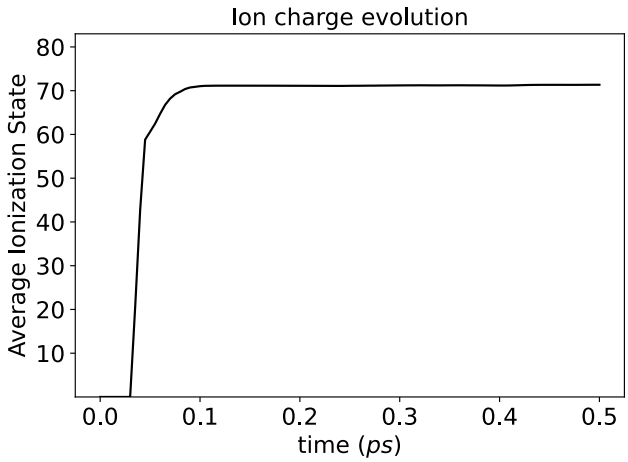

Figure 4.10: Ion charge evolution for the tungsten target. As can be seen, the maximum charge state is below the value of Z for the lead, meaning that not all the particles are fully ionized.

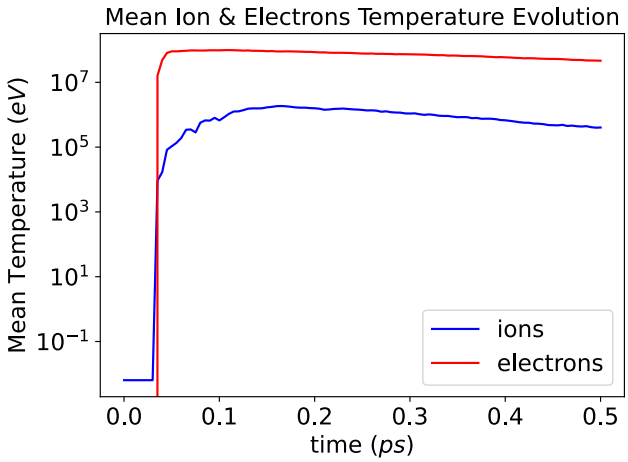

Figure 4.11: Electrons and ions temperature evolution for the lead target.

4.4 Tungsten Target

This simulation investigates the behavior of a tungsten target under various ionization mechanisms, including field ionization, multiphoton ionization, and barrier suppression ionization (BSI), as described theoretically in **chapter 1**. The objective here is to assess the impact of different ionization mechanisms on plasma formation. The first simulation involves a target with a thickness of 4 µm, a density

of $6.3 \times 10^{28}\,\mathrm{m}^{-3}$ at ambient temperature (293 K), and considers only field and multiphoton ionization. The target is irradiated by a perpendicularly incident laser beam with an intensity of $1 \times 10^{16}\,\mathrm{W\,cm}^{-2}$, a wavelength of 0.25 µm, and a pulse duration of 110 fs. Laser interaction results in target material ionization, with a steep increase in the average ionization state within the initial 40 fs. Subsequently, the curve's slope decreases, indicating reduced effectiveness in ionization through ionization and multiphoton ionization processes until 100 fs when the ionization state approaches a maximum of +64 (blue curve in **figure 4.12**).

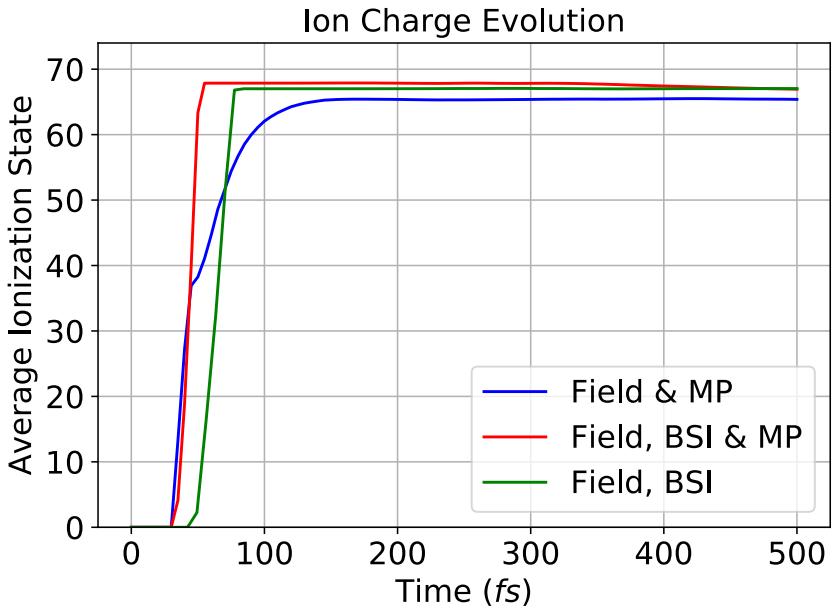

Figure 4.12: Average ionization state of tungsten for various simulations, each involving variations in the ionization processes.

The scenario differs when barrier suppression ionization (BSI) is introduced. In this case, the mean ion charge increases rapidly, as demonstrated by the red curve in **figure 4.12**. Additionally, the maximum ionization state achieved surpasses the previous scenario without BSI. Another simulation was conducted with multiphoton ionization turned off, as depicted in the green curve in **figure 4.12**. Here, it is evident that multiphoton ionization's effect on the final ionization state is negligible, as the maximum mean ion charge achieved is the same as the previous simulation, with a nearly identical steep increase. However, ionization phenomena commence later in time, indicating that multiphoton ionization plays a significant role in the simulation's initial stages, where multiple photons interacting with an electron's outer shell enable ionization before field ionization occurs.

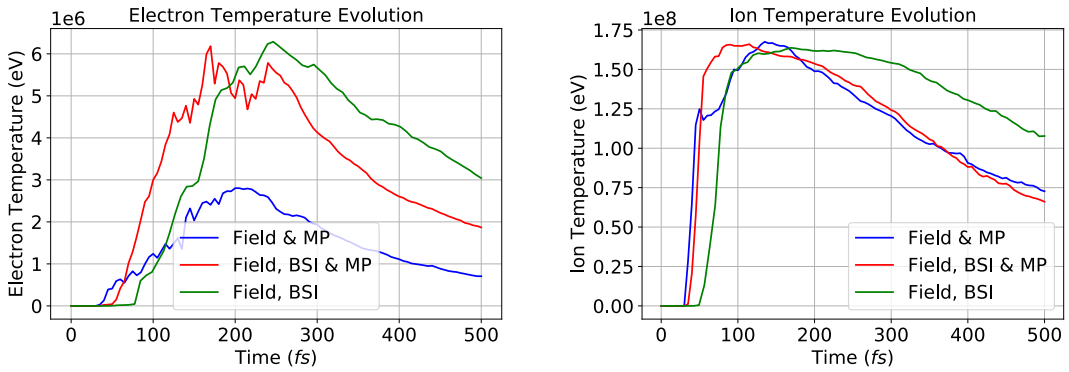

(a) **(b)**

Figure 4.13: Evolution of electron **(a)** and ion **(b)** temperatures for simulations involving different ionization processes.

Figure 4.13 displays temperature evolution in all different simulations. Specifically, electron temperature is lower when BSI is not activated. Nevertheless, the order of magnitude remains consistent. Regarding ion temperature, differences are insignificant, as the laser primarily heats electrons through various ionization mechanisms, enabling them to depart from the atoms, which subsequently become ionized. Once ionized, atoms may be heated through electron collisions, but this process is not significant within this time frame.

4.5 Proton-Boron Target

This section focuses on the analysis of a target that can serve as the "pitcher" in a pitcher-catcher configuration for Proton-Boron fusion. This configuration consists of two targets: a primary target (the "pitcher") irradiated by a laser and a secondary target (the "catcher") bombarded by a proton beam generated from the laser-pitcher interaction. Fusion reactions primarily occur in the secondary target, which is typically a boron sheet. The simulation here involves the interaction between a laser and a potential pitcher target composed of hydrogen and boron. Specifically, it examines a 1.5 µm boron foil coated on one side with a 0.2 µm layer of a polymeric material, namely, polystyrene $(C_8H_8)_n$ (as shown in **figure 4.14**). To set up the simulation, particle number densities were derived from material densities. In particular, for hydrogen has been used a particle density of $6 \times 10^{29}\,\mathrm{m}^{-3}$, for Carbon $5 \times 10^{28}\,\mathrm{m}^{-3}$ and for Boron $1 \times 10^{29}\,\mathrm{m}^{-3}$. To reduce computational time, the simulation domain was confined to the target space, significantly reducing the number of particles and cells needed. Furthermore, due to computational constraints, only one-dimensional analyses were conducted. As boundary conditions for all the simulation were applied a laser boundary on the left side (where the laser beam impacts), and an open boundary on the right side to make possible the expansion in space of the generated plasma.

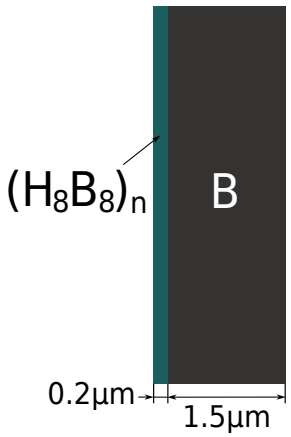

Figure 4.14: Pitcher target made of Boron, coated on the left side with a polystyrene substrate.

The laser employed in the simulations is a short-pulse laser characterized by a peak intensity of $1 \times 10^{20}\,\mathrm{W\,cm}^{-2}$, a duration of 500 fs, and a wavelength of 1.315 µm. The laser time profile is nearly square-shaped, with a rise/fall time of 0.5 ns. The polarization angle of the laser beam, as discussed in **chapter 1**, plays a crucial role in energy absorption by the target. Varying this angle was explored in the simulations. Additionally, the simulations considered variations in peak

temperature to assess their impact on the interaction.

As previously mentioned, the accuracy of these simulations depends on parameters like the number of cells and the number of particles per cell. The number of cells required can be determined by ensuring that the cell dimension is at least equal to the Debye length to capture spatial plasma variations accurately. From **equation** (1.2) the Debye length can be evaluated for the electrons, but the electron temperature is needed and it is a parameter not known a priori since it will be the results of the simulation. The same reasoning can be done for the density but, being at the denominator in **equation** (1.2), considering a solid density equal to the particle number density of the materials would lead to a conservative estimation of the Debye length. This is because an overestimation of the density brings to a lower value of the Debye length. For the temperature instead, from previous simulations, it has been seen that sooner after the interaction laser-target it reaches a value of the order of tens or hundred of MeV, for this reason it has been estimated a temperature of 0.5 MeV to evaluate the Debye length. From those considerations a number of cells equal to about 150 has been evaluated for the given domain. To be conservative a number of 200 cells has been used in the simulation. Regarding the number of particles per cell, although the exact number needed cannot be determined, experience from prior simulations suggests that 1000 particles per cell should yield reliable results. Increasing these parameters could enhance precision but would significantly extend computational time. However, the chosen parameters are sufficient to provide a reasonable approximation of plasma characteristics.

The first simulation of a proton-boron plasma had the initial conditions reported in **table 4.1**. Its objective was to simulate the interaction between a laser beam incident perpendicular to a solid target at room temperature (293 K).

Table 4.1: Simulation parameters

Laser Parameters		Domain Parameters	
Maximum Inensity	1×10^{20}	No of cells	200
duration	500fs	No of particles per cell	1000
polarization angle	0°	Final simulation time	500fs

Shortly after the laser beam interacted with the target, atoms within the system began ionizing due to field ionization processes, including multiphoton and BSI mechanisms. Given the short simulation time, collisional ionizations are non-relevant, so they have been neglected, moreover the laser intensity is high enough to promptly ionize the atoms comprising the target. **Figure 4.15** illustrates the ionization evolution in the system, where can be observed the prompt ionization of the atoms, which reaches complete ionization after a few femtoseconds.

The laser energy is absorbed by the wall, and besides causing ionization, it

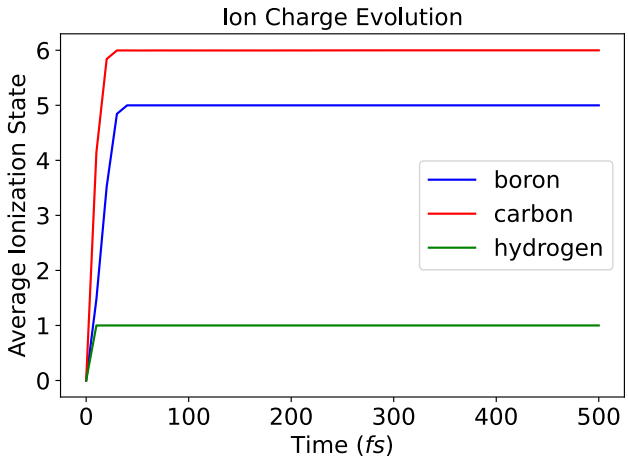

Figure 4.15: Ion charge evolution in the system for the target's constituent particles. It's evident that complete ionization occurs within a few femtoseconds.

leads to a swift rise in the system's temperature. Specifically, this temperature increase mainly affects the electrons, which not only break free from the atoms but also reach temperatures on the order of the MeV. In this simulation, the electron temperature reaches values between $0.1 - 1$ MeV (as shown in **figure 4.16a**). It's worth noting that the nuclei of the particles making up the material don't receive energy directly from the laser. Instead, they are heated through collisions with the electrons. As a result, the ion temperature is lower and typically falls within the range of 1 to 10 keV, as illustrated in **figure 4.16b**.

As the temperature rises, the plasma expands in space, reducing local density, and some of it is expelled from the system boundaries (**figure 4.18**). **Figure 4.17** displays the evolution of atom density in space and time, considering all ionization states. As illustrated, the plasma expands and shifts towards the right side of the system, with a portion exiting the system. This phenomenon is more clearly observed in **figure 4.19**, **figure 4.20** and **figure 4.21**, where the particle density at the end of the simulation (500 fs) is reported (panel b) along with the ions evolution (panel a). Each picture represents a different atom (**figure 4.19** Hydrogen, **figure 4.20** Carbon and **figure 4.21** Boron). From these images, it's evident that by the end of the simulation, the majority of particles have become fully ionized, and the number density of less ionized particles is negligible. The same holds for the evolution in time of the particles (panel a of each figure), where it can be seen how the majority of the particles are quickly fully ionized and only a small fraction of them remain in a lower charge state. This observation aligns with what's depicted in **figure 4.15**, which shows the average ionization state. Furthermore, the particle density in the system is lower than initially, indicating

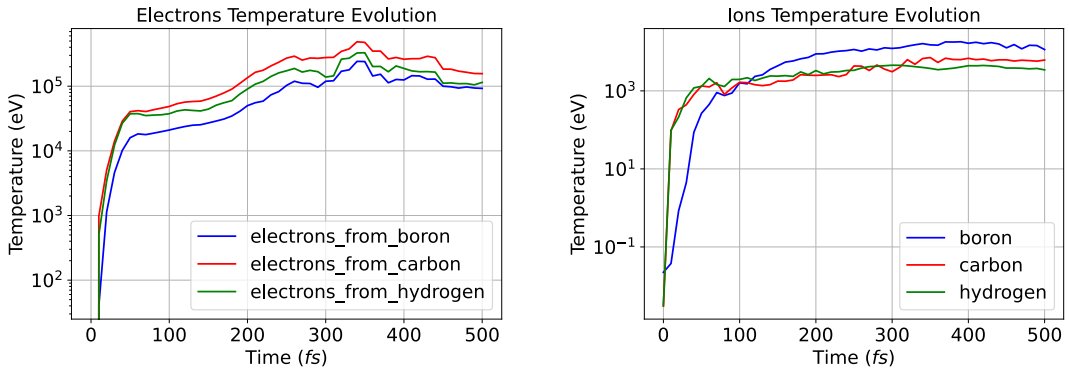

(a) **(b)**

Figure 4.16: Temperature changes within the system. Panel (a) displays the temperature of the electrons derived from the different atoms, while panel (b) demonstrates the temperature evolution of different ions, regardless of their ionization state. It's noticeable that there exists a significant disparity in temperature between these two species, spanning two orders of magnitude.

that a fraction of the initial particles has exited the system.

The temperature evolution reflects the kinetic energy of the particles and, consequently, the energy absorbed by the laser. it is interesting to note the fraction of laser energy absorbed by the particles, as reported in Figure 8. To calculate this energy fraction, the energy associated with the particles was computed as $3/2K_BT$ multiplied by the particle density and volume. Since this is a one-dimensional simulation, it was multiplied only by the length of the domain. Once the particles' energy has been evaluated, then the difference in energy with respect to the initial condition has been calculated and then divided by the laser energy to obtain the absorption fraction. The results, as depicted in **figure 4.22**, reveal that only a small portion of the laser energy is absorbed by the particles. Specifically, the maximum absorption occurs at around 350 femtoseconds, where only 8% of the laser energy is absorbed by the particles.

Additional simulations were conducted and their results were compared to the previous one. It is known that increasing the incidence angle of the laser beam leads to a greater absorption of laser energy by the target thanks to resonance phenomena. Consequently, two simulations were executed, each with a different polarization angle (45° and 60°), while keeping all other parameters constant. The simulation outcomes in terms of energy absorption are presented in **figure 4.23a** along with the fraction of ions leaving the system. The figures show the comparison of three different simulations which differ only by the laser polarization angles (0°, 45° and 60°). **figure 4.23a** illustrates how an increase in the polarization angle

results in higher laser energy absorption by the target. Specifically, when using a 60° angle, the maximum absorbed energy fraction by the laser is approximately 16%, nearly twice that of cases with 0° and 45° polarization angles. Concerning the ejection of particles from the system, the maximum number of ions leaving the system boundaries is observed when the polarization angle is 45°. This is noteworthy because the goal of a pitcher target is to generate a beam of accelerated particles, so an increase in the number of particles exiting the system is a desirable

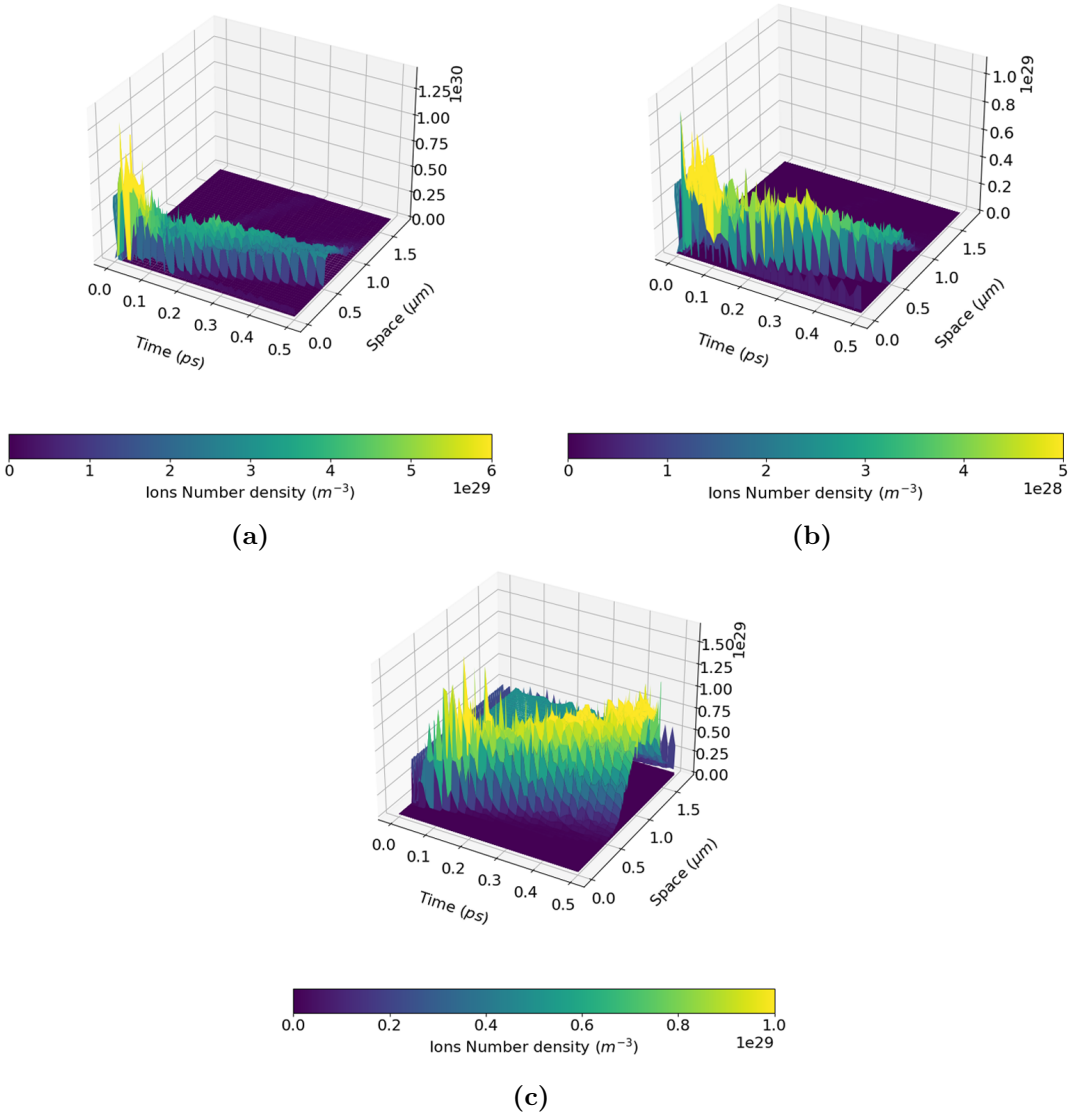

Figure 4.17: Spatial and temporal evolution of density for hydrogen **(a)**, carbon **(b)**, and boron **(c)**.

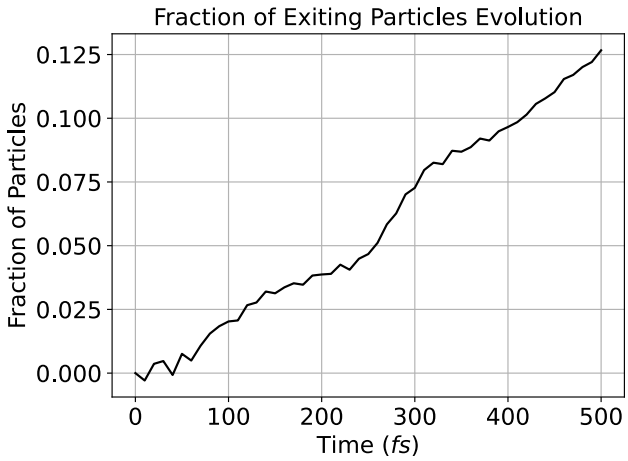

Figure 4.18: Evolution of the fraction of particles exiting the system. At the end of the simulation,12.5% of the initial particles have exited the system.

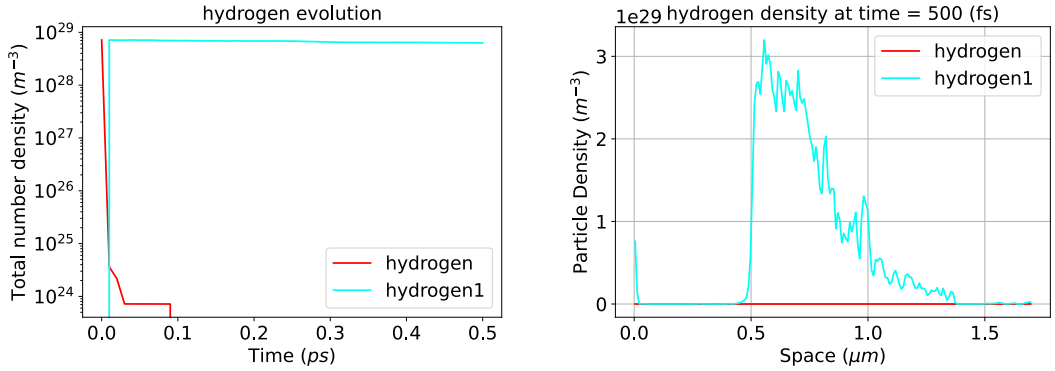

(a) **(b)**

Figure 4.19: Evolution of hydrogen atoms. In particular, in panel (a), the evolution of the hydrogen atoms is shown, where it can be observed how neutral hydrogen is promptly ionized to hydrogen +1. In panel (b), a picture of the final time frame is shown, displaying the particle density in the system, which mainly consists of hydrogen +1.

outcome. However, it's crucial to note that the simulation duration is limited to 500 fs, and the number of exiting particles will likely continue to rise with time. Therefore, the precise trend of these curves may evolve over a longer simulation period.

The average energy associated with emitted particles is presented in the following figures. As evident from the graphs, the mean kinetic energy of the ejected particles falls within the range of $0.5 - 2$MeV, depending on the type of particles.

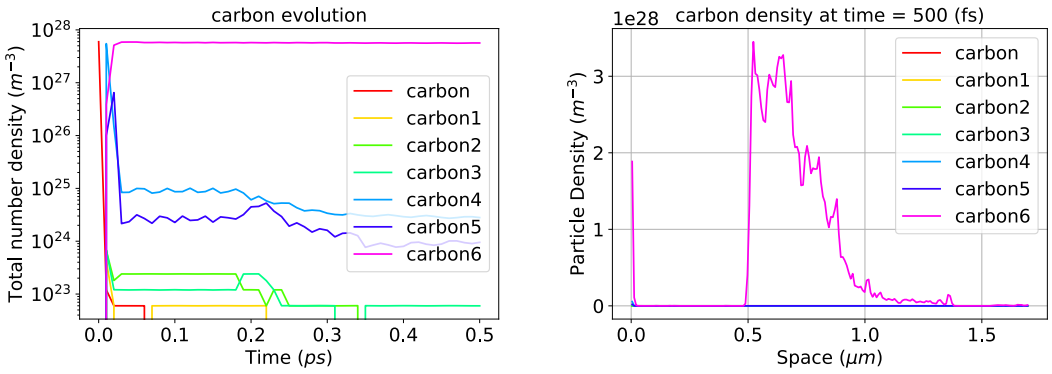

(a) **(b)**

Figure 4.20: Evolution of carbon atoms (a). Here, it can be seen how neutral hydrogen is promptly ionized to hydrogen +1. In panel (b), there is a picture of the final time frame, displaying the particle density in the system, which is primarily composed of carbon +6.

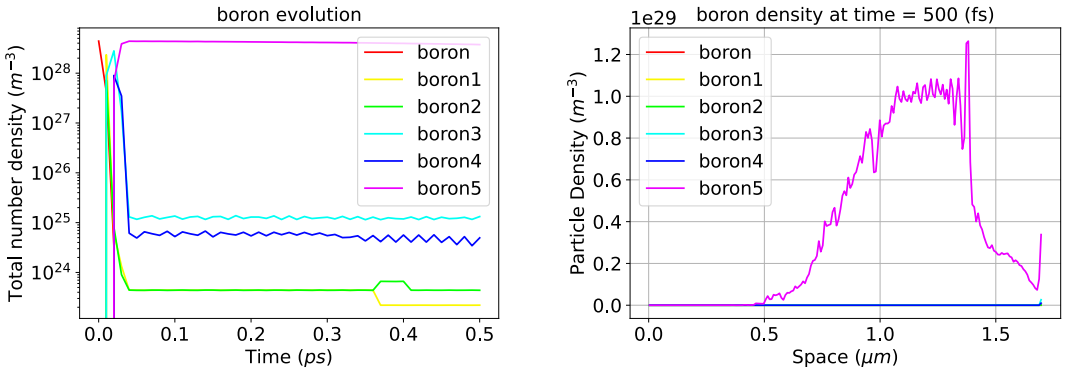

(a) **(b)**

Figure 4.21: Evolution of boron atoms (a). In figure, one can observe how neutral boron promptly becomes ionized to boron +1. In panel (b), there is a depiction of the final time frame, displaying the particle density in the system, which consists mainly of boron +5.

Figure 4.24a and **figure 4.24b** depict, respectively, the kinetic energy of ions and electrons derived from hydrogen. **Figure 4.24a** and **figure 4.24b** represent the kinetic energy of ions and electrons derived from hydrogen. Meanwhile, **figures 4.24c** and **4.24d** illustrate the kinetic energy of ions and electrons originating from carbon. Finally, **figures 4.24e** and **4.24f** showcase the kinetic energy of ions and electrons originating from boron.

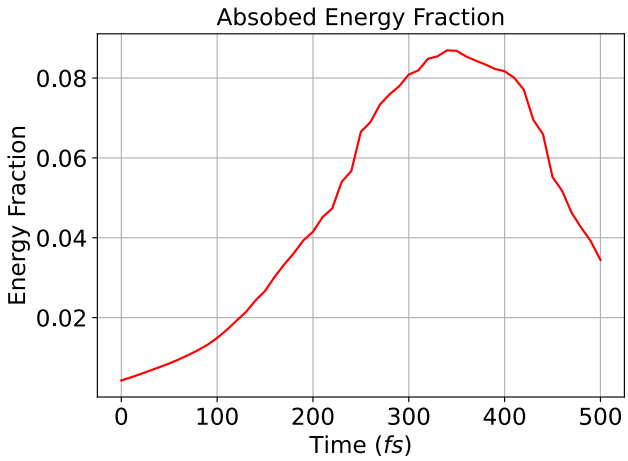

Figure 4.22: Fraction of laser energy absorbed by the target's particles.

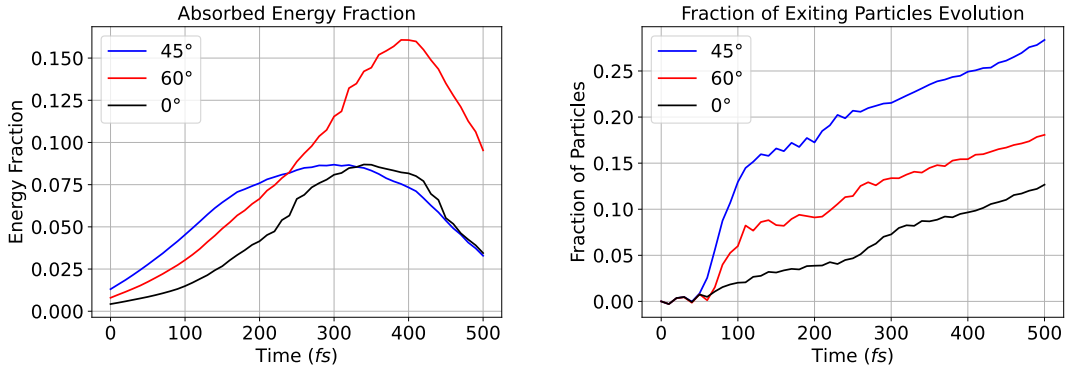

(a) **(b)**

Figure 4.23: In panel (a), the evolution of the laser energy fraction absorbed by the target is displayed. It's evident that the maximum energy absorption occurs when using a polarization angle of 60°. In panel (b), the fraction of particles exiting the system over time is depicted. Specifically, it can be observed that the highest fraction of particles ejected from the system boundaries is achieved when employing a polarization angle of 45°.

To highlight the evolution of the system beyond 500fs, another simulation was conducted by extending the simulation time domain. In this simulation, a laser beam with a maximum intensity of $1 \times 10^{20}\,\mathrm{W^2\,cm^{-1}}$, a polarization angle of 60°, and a pulse duration of 500 fs was employed while keeping all other simulation parameters constant, with the exception of the simulation time which has been increased to 1 ps. The simulation showed an absorption fraction similar to the

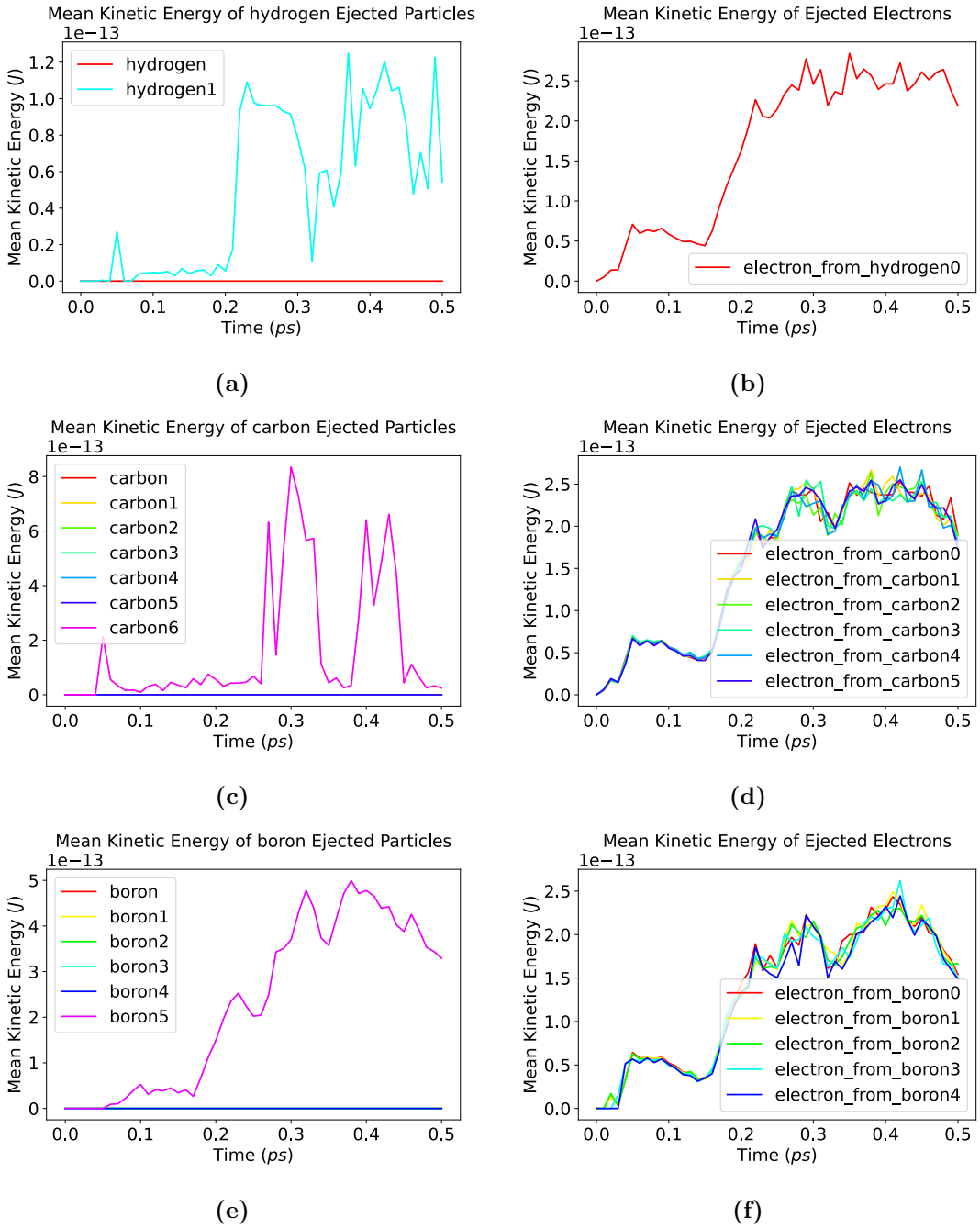

Figure 4.24: Mean kinetic energy of the different ejected particles.

previous one, as only the time domain was altered. However, the fraction of particles expelled from the simulation boundaries increased at a steeper rate after 500 fs, eventually reaching 80% by the end of the simulation (as shown in **figure 4.25**). Consequently, it cannot be definitively stated, based solely on **figure 4.23b**, that the number of ejected particles would be greater with a polarization angle of 45°.

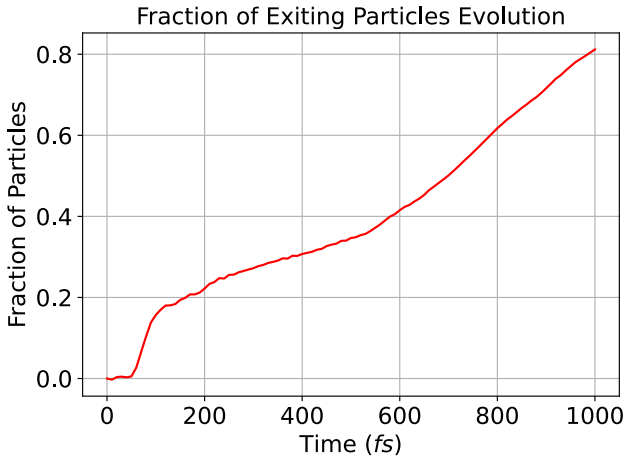

Figure 4.25: Progression of the particle fraction expelled from the simulation boundary, considering a polarization angle of 60° and a time domain of 1ps. After 500fs, the fraction of particles exiting the system exhibits a steeper increase.

To investigate how laser intensity impacts plasma characteristics, simulations were conducted with varying laser intensities: one at $I_{max} = 1 \times 10^{18}\,\mathrm{W^2\,cm^{-1}}$ and another at $I_{max} = 1 \times 10^{16}\mathrm{W/cm^2}$. The latter simulation did not exhibit any ionization within the first 500 fs, indicating that a laser with an intensity of $1 \times 10^{16}\,\mathrm{W^2\,m^{-1}}$ and a pulse duration of 500 fs is insufficient to fully ionize the target material. In contrast, the simulation with a maximum intensity of $1 \times 10^{18}\,\mathrm{W^2\,cm^{-1}}$ managed to ionize the material, though it still did not achieve complete ionization of boron or carbon atoms within the initial 500 fs. The results are presented in the following figures. **Figure 4.26** illustrates the evolving average ionization state, clearly indicating that the atoms are not fully ionized. **Figure 4.27**, on the other hand, displays the evolution of ion number density for each species.

With lower laser energy, it is expected a lower temperature evolution both for ions and electrons. **figure 4.28a** illustrates the temperature evolution for both ions and electrons, emphasizing that the maximum temperature for electrons is approximately 1 keV, which is at least two orders of magnitude lower than the case with $I_{max} = 1 \times 10^{20}\,\mathrm{W^2\,cm^{-1}}$. The same trend is observed for ions (**figure 4.28b**), where the maximum temperature reaches 10eV.

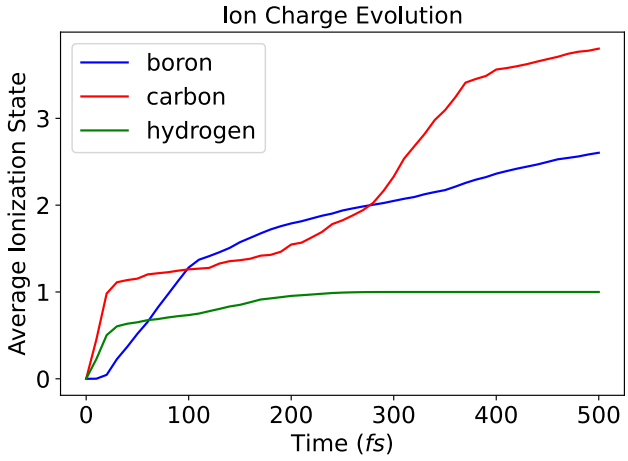

Figure 4.26: Evolution of the average ionization state for the simulation with $1 \times 10^{18}\,\mathrm{W^2\,cm^{-1}}$ and pulse duration of 500 fs. In this conditions, the atoms are not fully ionized.

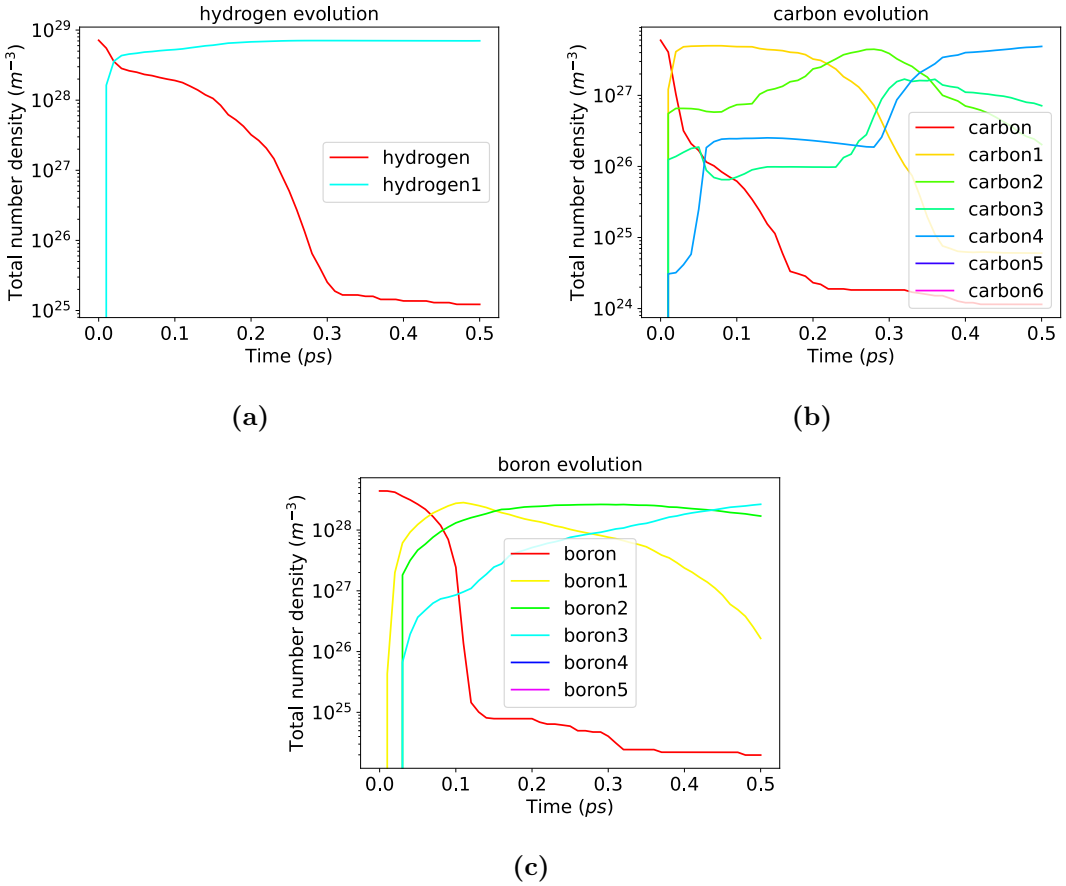

Figure 4.27: Evolution of ions for each species. As observed in the upper images, boron+5 and carbon+6 ions are not formed during the laser pulse.

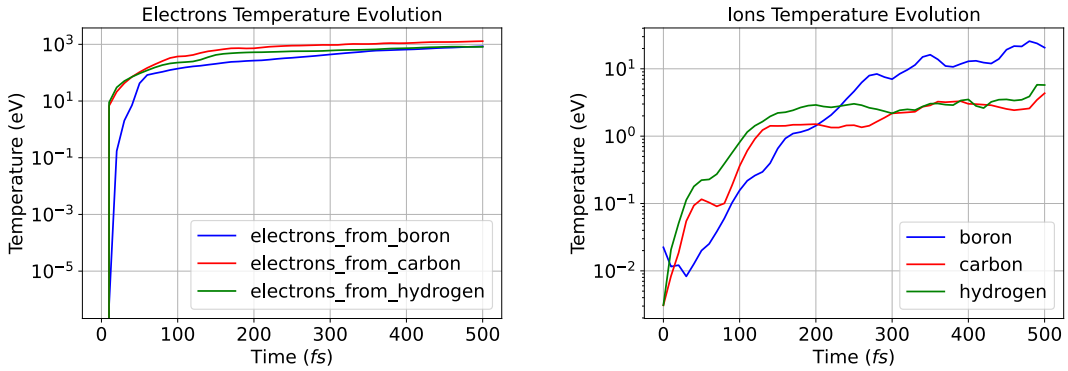

(a) **(b)**

Figure 4.28: Temperature evolution in the system for both electrons **(a)** and ions **(b)**. The temperatures reached are significantly lower compared to the case with $I_{max} = 1 \times 10^{20}\,\mathrm{W^2\,cm^{-1}}$.

Chapter 5

Conclusions and perspective

The work presented here aimed to computationally analyze the interaction between laser and matter, with a particular focus on proton-boron fusion. Initially, it explored the physical phenomena characterizing this interaction, primarily concentrating on the mechanisms of laser-induced matter ionization. Subsequently, it has been examined a computational model able to correctly reproduce the interaction between laser and matter, such a model is a PIC (Particle in cell) code. This phase involved an in-depth examination of the key features of the model and the computational methods required to solve its fundamental equations.

The next step involved actual computational analysis. Initially, the goal was to replicate literature results to verify the accuracy of the obtained outcomes. Although some information necessary for setting up the simulations was missing, it was possible to replicate the results to a significant extent. While some graphs did not precisely match the originals, the physical behavior of the system remained consistent.

The analysis then progressed to investigate various target materials to study their interaction with the laser, revealing how changes in laser parameters alter the conditions of the generated plasma. Crucial parameters included laser intensity, pulse duration, and the polarization angle of the laser beam. For instance, certain materials, like cesium, required higher laser intensities for complete ionization compared to materials like aluminum or tungsten. Additionally, by focusing on a tungsten target, the impact of different ionization processes on ion production within the system was examined. It was observed that the barrier-suppression ionization (BSI) plays a significant role, although it occurs temporally later than multiphoton ionization, as it demands higher energy to become significant.

Subsequently, simulations were conducted to analyze a potential primary target in a pitcher-catcher configuration for proton-boron fusion. The generated plasma was examined, particularly when employing a laser with a maximum intensity of $1 \times 10^{20}\,\mathrm{W/cm^2}$, a pulse duration of 500 fs, and a polarization angle of 60°,

resulting in maximum energy absorption and electron temperature. Although the temperature variation was not substantial, enhanced target absorption could lead to more efficient interaction, potentially allowing for a reduction in laser intensity.

Furthermore, it was observed that within a timescale on the order of 1 ps, approximately 80% of particles were expelled from the considered system with energies in the MeV range. This observation is of significance, as the primary aim of a pitcher target is to generate a high-energy proton beam, which will subsequently interact with a secondary target (the catcher) to initiate proton-boron fusion.

The work accomplished has successfully achieved the predetermined goals by analyzing the interaction between laser and matter for various targets. In particular, concerning the proton-boron target, one of the potential configurations for generating high-energy proton beams has been considered. However, there are many other targets that could serve the same purpose, possibly yielding better results in terms of laser energy absorption. These targets consist of lightweight elements containing hydrogen and boron but can exist in various states. For instance, porous targets, typically composed of a porous substrate that enhances energy absorption, are particularly interesting in the context of inertial confinement fusion. Due to their internal porous structure, which varies from one foam to another, experiments become non-reproducible. In such cases, computational studies become essential, which could be conducted using PIC models, possibly coupled with fluid dynamic models for characterizing the generated plasma.

Bibliography

[1] Dimitri Batani, Daniele Margarone, and Fabio Belloni. «Advances in the study of laser-driven Proton-Boron Fusion». In: *Journal Name* Volume Number (2023), Page Numbers. DOI: 10.12345/your-doi-number (cit. on p. v).

[2] URL: https://wallpaperaccess.com/4k-ultra-hd-lightning-phone. (accessed: June 2023) (cit. on p. 1).

[3] URL: https://getwallpapers.com/wallpaper/full/8/3/e/198252.jpg. (accessed: June 2023) (cit. on p. 1).

[4] URL: https://it.wikipedia.org/wiki/Plasma_(fisica)#/media/File:HeTube.jpg. (accessed: June 2023) (cit. on p. 1).

[5] Hideaki Takabe. *The Physics of Laser Plasma and Applications*. Series in Plasma Science and Technology. Springer, 2018. ISBN: 978-3-319-74384-5 (cit. on pp. 2, 10–12).

[6] I.H.Hutchinson. *Introduction to Plasma Physics*. Accessed: June 2023. URL: http://silas.psfc.mit.edu/introplasma/ (cit. on p. 2).

[7] Francis F. Chen. *Introduction to Plasma Physics*. Springer, 2016 (cit. on pp. 2–4).

[8] Alexander Piel. *Plasma Physics: An Introduction to Laboratory Space and Fusion Plasma*. Springer, 2010 (cit. on pp. 3, 4).

[9] C.J. Joachain, N.J. Kylstra, and R.M. Potvliege. *Atoms in Intense Laser Fields*. Cambridge University Press, 2003 (cit. on pp. 4, 6).

[10] Igor Jovanovic. «Chirped-Pulse Amplification Ultrahigh peak power production from compact short-pulse laser systems». In: *Wiley-VCH Verlag GmbH & Co. KGaA, Weinheim* (2010) (cit. on p. 5).

[11] URL: https://commons.wikimedia.org/wiki/File:History_of_laser_intensity.svg. (accessed: June 2023) (cit. on p. 6).

[12] URL: https://en.wikipedia.org/wiki/Chirped_pulse_amplification#/media/File:Chirped_pulse_amplification.png. (accessed: June 2023) (cit. on p. 7).

[13] Eugene G Gamaly. *Femtosecond Laser-Matter Interaction: Theory, Experiments and Applications*. Springer Science & Business Media, 2011 (cit. on pp. 7, 9).

[14] URL: http://experimentationlab.berkeley.edu/sites/default/files/MOT/Gaussian-Beam-Optics.pdf. (accessed: June 2023) (cit. on pp. 8, 9).

[15] Christopher C. Davis. *Lasers and Electro-optics*. Cambridge University Press, 2014. DOI: https://doi.org/10.1017/CBO9781139016629 (cit. on p. 9).

[16] Gabriel Laufer. *Introduction to Optics and Lasers in Engineering*. Cambridge University Press, 2012. DOI: https://doi.org/10.1017/CBO9781139174190 (cit. on p. 9).

[17] A. E. Siegman. «How to (Maybe) Measure Laser Beam Quality». In: *DPSS (Diode Pumped Solid State) Lasers: Applications and Issues*. Optica Publishing Group, 1998, MQ1. DOI: 10.1364/DLAI.1998.MQ1. URL: https://opg.optica.org/abstract.cfm?URI=DLAI-1998-MQ1 (cit. on p. 9).

[18] Geoffrey J. Pert. *Foundations of Plasma Physics for Physicists and Mathematicians*. Department of Physics, University of York, UK (cit. on pp. 9–11, 14).

[19] Peter Mulser and Dieter Bauer. *High Power Laser–Matter Interaction*. Springer, 2010 (cit. on pp. 10, 14).

[20] D. Bauer. «Plasma formation through field ionization in intense laser–matter interaction». In: () (cit. on p. 11).

[21] I. Yu. Kostyukov and A. A. Golovanov. «Field ionization in short and extremely intense laser pulses». In: (2018) (cit. on p. 11).

[22] N. B. Delone and V. P. Krainov. «Tunneling and barrier-suppression ionization of atoms and ions in a laser radiation field». In: () (cit. on p. 12).

[23] Patrick Vanraes and Annemie Bogaerts. «Laser-induced excitation mechanisms and phase transitions in spectrochemical analysis – Review of the fundamentals». In: *Spectrochimica Acta Part B: Atomic Spectroscopy* 179 (2021), p. 106091. DOI: 10.1016/j.sab.2021.106091 (cit. on p. 13).

[24] P. Gibbon and E. Forster. «Short-pulse laser–plasma interactions». In: *Plasma Phys. Control. Fusion* 38.6 (1996), p. 769 (cit. on p. 14).

[25] Mahdavi and Ghazizadeh. «Linear Absorption Mechanisms in Laser Plasma interactions». In: *Journal of Applied Sciences* () (cit. on p. 14).

[26] J.W. Eastwood R.W. Hockney. *Computer Simulation using particles*. CRC Press, 1st edition, 1989 (cit. on pp. 16, 18, 19, 22, 26).

[27] C.K Langdon Birdsall. *Plasma physics via computer simulation*. Series in Plasma Physics and Fluid Dynamics. CRC Press, 2004 (cit. on p. 18).

[28] Okuda H. C.K. Birdsall. «Collision in a plasma of finite-size particles». In: *Physical Review Letters* 24.19 (1970), pp. 920–923. DOI: 10.1103/PhysRevLett.24.920 (cit. on p. 18).

[29] T D Arber et al. «Contemporary particle-in-cell approach to laser-plasma modelling». In: *Plasma Physics and Controlled Fusion* 57.11 (2015). DOI: 10.1088/0741-3335/57/11/113001 (cit. on pp. 20, 26–28, 30, 32, 35, 38).

[30] Bell A. R. Arber T. D. Kirk J. G. «Development of a one-dimensional particle-in-cell code with adaptive mesh refinement for kinetic plasma simulations.» In: *Journal of Computational Physics* 193.1 (2003), pp. 1–27. DOI: 10.1016/j.jcp.2003.07.008 (cit. on p. 20).

[31] A. D'Angola G. Colonna. *Plasma modelling - Methods and applications*. IOP Series in Plasma Physics. IOP Publishing, Bristol, UK, 2022 (cit. on p. 21).

[32] J.V. Shebalin. «A spectral algorithm for solving the relativistic Vlasov-Maxwell equations». In: *NASA Technical Reports Server* (1999) (cit. on p. 22).

[33] Giovanni Lapenta. «Particles simulations of space weather». In: *Journal of Computational Physics* 231 (2012), pp. 795–821. DOI: 10.1016/j.jcp.2011.03.035 (cit. on pp. 22, 24).

[34] Aimilios Mouziouras. «Comparison of EPOCH and SMILEI Particle-In-Cell codes in laser driven particle acceleration PIC simulations for laser-plasma interaction». In: (2019). DOI: 10.13140/RG.2.2.14651.85286 (cit. on pp. 24, 27).

[35] G. Zuccaro k. Noguchi C. Tronci and G. Lapenta. «Formulation of the relativistic moment implicit particle-in-cell method». In: *Pysics of Plasma* 14 (2007). DOI: 10.1063/1.2721083 (cit. on p. 24).

[36] «On the Boris solver in particle-in-cell simulation». In: *Pysics of Plasmas* 25 (2018). DOI: 10.1063/1.5051077 (cit. on p. 26).

[37] Kane S. Yee. «Numerical Solution of Initial Boundary Value Problems Involving Maxwell's Equations in Isotropic Media». In: *IEEE Transactions on Antennas and Propagation* 14 (3 1966), pp. 302–307. DOI: 10.1109/TAP.1966.1138693 (cit. on p. 27).

[38] T. Zh Esirkepov. «Exact charge conservation scheme for particle-in-cell simulation with an arbitrary form-factor». In: *Computer Physics Communications* 135.2 (2001), pp. 144–153 (cit. on p. 28).

[39] *EPOCH Documentation*. https://epoch-pic.github.io/documentation.html. 2022 (cit. on p. 30).

[40] Y Sentoku and A Kemp. «Numerical methods for particle simulations at extreme densities and temperatures: Weighted particles, relativistic collisions and reduced currents». In: *Computer Physics Communications* 179.8 (2008), pp. 557–565 (cit. on p. 30).

[41] F Pérez, L Gremillet, A Decoster, M Drouin, and E Lefebvre. «Improved modelling of relativistic collisions and collisional ionization in particle-in-cell codes». In: *Physics of Plasmas* 19.8 (2012). DOI: 10.1063/1.4742167 (cit. on p. 30).

[42] M. V. Ammosov, N. B. Delone, and V. P. Krainov. «Tunnel ionization of complex atoms and of atomic ions in an alternating electromagnetic field». In: *Soviet Physics Journal of Experimental and Theoretical Physics* 64 (1986), pp. 1191–1194 (cit. on p. 30).

[43] M. V. Ammosov, N. B. Delone, and V. P. Krainov. «Multiphoton Processes in Atoms». In: *Advances in Atomic, Molecular, and Optical Physics*. Vol. 13. Elsevier, 1994, pp. 90–94 (cit. on p. 30).

[44] A. Haque, M. Alfaz Uddin, A. Basak, K. Karim, B. Saha, and F. Malik. «Phys. Scr.» In: 74 (2006), p. 377. DOI: 10.1088/0031-8949/74/3/005 (cit. on p. 30).

[45] Christopher P Ridgers, John G Kirk, Romain Duclous, Thomas G Blackburn, Christopher S Brady, Keith Bennett, Tony D Arber, and Anthony R Bell. «Modelling gamma-ray photon emission and pair production in high-intensity laser-matter interactions». In: *Journal of Computational Physics* 260 (2014), pp. 273–285. DOI: 10.1016/j.jcp.2013.12.016 (cit. on p. 31).

[46] R Duclous, JG Kirk, and AR Bell. «Monte Carlo calculations of pair production in high-intensity laser-plasma interactions». In: *Plasma Physics and Controlled Fusion* 53.1 (2011), p. 015009. DOI: 10.1088/0741-3335/53/1/015009 (cit. on p. 31).